remote sensing

MDPI

Article

A Theoretical Analysis for Improving Aerosol-Induced CO_2 Retrieval Uncertainties Over Land Based on TanSat Nadir Observations Under Clear Sky Conditions

Xi Chen [1], Yi Liu [1,2,3], Dongxu Yang [1,2], Zhaonan Cai [1], Hongbin Chen [1] and Maohua Wang [2,*]

1 Key Laboratory of Middle Atmosphere and Global Environment Observation, Institute of Atmospheric Physics, Chinese Academy of Sciences, Beijing 100029, China; chenxilageo@mail.iap.ac.cn (X.C.); liuyi@mail.iap.ac.cn (Y.L.); yangdx@mail.iap.ac.cn (D.Y.); caizhaonan@mail.iap.ac.cn (Z.C.); chb@mail.iap.ac.cn (H.C.)
2 Shanghai Advanced Research Institute, Chinese Academy of Sciences, Shanghai 201210, China
3 University of Chinese Academy of Sciences, Beijing 100049, China
* Correspondence: wangmh@sari.ac.cn

Received: 8 March 2019; Accepted: 1 May 2019; Published: 5 May 2019

check for updates

Abstract: Aerosols significantly affect carbon dioxide (CO_2) retrieval accuracy and precision by modifying the light path. Hyperspectral measurements in the near infrared and shortwave infrared (NIR/SWIR) bands from the generation of new greenhouse gas satellites (e.g., the Chinese Global Carbon Dioxide Monitoring Scientific Experimental Satellite, TanSat) contain aerosol information for correction of scattering effects in the retrieval. Herein, a new approach is proposed for optimizing the aerosol model used in the TanSat CO_2 retrieval algorithm to reduce CO_2 uncertainties associated with aerosols. The weighting functions of hyperspectral observations with respect to elements in the state vector are simulated by a forward radiative transfer model. Using the optimal estimation method (OEM), the information content and each component of the CO_2 column-averaged dry-air mole fraction (XCO_2) retrieval errors from the TanSat simulations are calculated for typical aerosols which are described by Aerosol Robotic Network (AERONET) inversion products at selected sites based on the *a priori* and measurement assumptions. The results indicate that the size distribution parameters (r_{eff}, v_{eff}), real refractive index coefficient of fine mode (a_r^{f}) and fine mode fraction (fmf) dominate the interference errors, with each causing 0.2–0.8 ppm of XCO_2 errors. Given that only 4–7 degrees of freedom for signal (DFS) of aerosols can be obtained simultaneously and CO_2 information decreases as more aerosol parameters are retrieved, four to seven aerosol parameters are suggested as the most appropriate for inclusion in CO_2 retrieval. Focusing on only aerosol-induced XCO_2 errors, forward model parameter errors, rather than interference errors, are dominant. A comparison of these errors across different aerosol parameter combination groups reveals that fewer aerosol-induced XCO_2 errors are found when retrieving seven aerosol parameters. Therefore, the model selected as the optimal aerosol model includes aerosol optical depth (AOD), peak height of aerosol profile (H_p), width of aerosol profile (H_w), effective variance of fine mode aerosol (v_{eff}^{f}), effective radius of coarse mode aerosol (r_{eff}^{c}), coefficient a of the real part of the refractive index for the fine mode and coarse mode (a_r^{f} and a_r^{c}), with the lowest error of less than 1.7 ppm for all aerosol and surface types. For marine aerosols, only five parameters (AOD, H_p, H_w, r_{eff}^{c} and a_r^{c}) are recommended for the low aerosol information. This optimal aerosol model therefore offers a theoretical foundation for improving CO_2 retrieval precision from real TanSat observations in the future.

Keywords: TanSat; aerosol; DFS; error; CO_2

1. Introduction

The concentration of carbon dioxide (CO_2) in the atmosphere has been rapidly increasing since the 1750s, and CO_2 has been recognized as one of the most significant greenhouse gases responsible for global warming [1]. To understand and mitigate anthropogenic CO_2 emissions, regional carbon flux estimation is required for identifying CO_2 sources and sinks. State-of-the-art data assimilation methods, coupled with modern atmospheric transport modeling, can provide reliable estimates of CO_2 surface flux when using a high-quality measurement dataset [2]. Unfortunately, limits on our understanding of CO_2 emissions and uptake lead to large uncertainties in climate change research due to a lack of accurate and continual measurements with global coverage. The cutting-edge technologies utilized in the manufacturing of spectrometers onboard satellites provide an opportunity to improve the global measurement coverage. The path finder instrument, Scanning Imaging Absorption Spectrometer for Atmospheric Chartography (SCIAMACHY), which is onboard the European Space Agency's (ESA) ENVISAT, first detected CO_2 signals in the atmosphere using near infrared (NIR) and shortwave infrared (SWIR) bands which are sensitive to near surface CO_2 concentration, providing reliable observations of global CO_2 column-averaged dry-air mole fractions (XCO_2). The Japanese satellite, Greenhouse Gases Observing Satellite (GOSAT), was successfully launched in 2009 and showed a good performance in-orbit [3,4]. The XCO_2 retrieved from GOSAT measurements indicated precision better than 1% [5], which significantly enhanced the knowledge of regional CO_2 surface fluxes [6,7]. In July 2014, NASA launched the Orbiting Carbon Observatory-2 (OCO-2), which started to provide XCO_2 data products with high quality to the public [8,9]. The Chinese carbon dioxide observation satellite mission (TanSat) began in 2010 and was launched on 22 December 2016 [10–12]. Recent studies have released preliminary XCO_2 maps produced from TanSat measurements [13].

Improvements in the accuracy and precision of XCO_2 retrievals will significantly contribute to reducing uncertainty in the estimation of CO_2 fluxes. Ideally, the accuracy of XCO_2 should be better than 0.3% (~1 ppm) to guarantee the accuracy of the regional surface carbon flux calculations [14]. Scattering in the atmosphere from aerosols and clouds could introduce serious errors in retrievals because the scattering changes the light path and results in different absorption by the gases. Aben, et al. [15] concluded that uncertainty in the aerosol optical depth (AOD) should be controlled to within 0.05 to maintain the total error in the CO_2 column at less 0.5%. The simulations of OCO-2 observations and the corresponding linear error analysis indicated that the uncertainties in the aerosols were among the dominant error sources encountered in CO_2 retrievals [16,17].

Additionally, according to error analyses of simulated GOSAT observations, imperfectly characterized clouds and aerosols are the dominant sources of error encountered during XCO_2 retrievals [18,19], meaning that to approach high-precision CO_2 retrieval, a method of eliminating uncertainty in aerosol property calculations is required, especially in heavily air-polluted areas. Synchronous aerosol measurements have been highly recommended for several satellite missions to reduce the retrieval errors from aerosol and cloud scattering. For instance, TanSat carries an ancillary instrument, the Clouds and Aerosol Polarimetric Imager (CAPI), which aims to improve the knowledge of aerosol and cloud contamination by obtaining simultaneous measurements with the Atmospheric Carbon Dioxide Grating Spectrometer (ACGS). Previous studies have reported that aerosol microphysical property information, e.g., aerosol volume concentration and size parameters, can be obtained from CAPI measurements [20,21]. The *a priori* of aerosol model parameters in TanSat CO_2 retrieval will be improved by using CAPI measurements.

However, this simultaneous aerosol measurement depends on the mission budget and instrument design and is not commonly achieved for each satellite. Under this circumstance, following the retrieval by the optimal estimation method (OEM), the a priori assumption of aerosol parameters becomes important when there is a lack of information in the measurements. A time- and location-specific 3D aerosol status provided by the chemical transport model (CTM) is an alternative option to obtain first estimates of aerosol parameters that are close to reality to reduce retrieval errors from the aerosol parameter uncertainty. For example, in the Japanese National Institute for Environmental Studies full physical (NIES-FP) retrieval algorithm of GOSAT, for every observed day, AOD computed through the Spectral Radiation-Transport Model for Aerosol Species (SPRINTARS) is used as a priori value. Additionally, during the XCO_2 retrieval process, the AODs of both fine and coarse-mode aerosols are retrieved synchronously, while aerosol type and size distribution data are provided by external sources [5,22]. In the NASA Atmospheric CO_2 Observations from Space (ACOS) retrieval algorithm for OCO-2 [19], three aerosol and profile parameters (AOD at 755 nm, peak height, and width of profile) for five types of scattering particles, including liquid water and ice clouds, two dominant tropospheric aerosols, and one stratospheric aerosol, have been corrected synchronously as the state vector. Both tropospheric aerosols were selected from those available in the Modern-Era Retrospective Analysis for Research and Applications (MERRA) reanalysis system, i.e., dust, smoke, sea salt, sulfate aerosol, organic carbon, and black carbon, which constitute the two largest fractions of AOD based on monthly averaged MERRA data. In general, there are two types of aerosol solutions which can be used in CO_2 retrieval algorithms. Both of them have advantages and disadvantages. One type uses a combination of multiple types of aerosols and retrieves the profile and loading of each type, such as in ACOS, NIES-FP and University of Leicester full physical (UoL-FP) algorithms [18,19,22,23], which are more related to the CTM model simulation. The other aerosol combination is depicted by an empirical aerosol model, namely, the wavelength dependence of aerosol optical properties (RemoTeC algorithm from institutes in Netherland and Germany and Institute of Atmospheric Physics, Chinese Acedemy of Sciences (IAPCAS)-TanSat algorithm from China), which show more dynamic ranges of aerosol microphysical parameters (e.g., size distribution) [10,24,25]. Although Gamma distribution is used as the aerosol size distribution in some CO_2 algorithms (such as RemoTeC), the bimodal size distribution aerosol model, which has been widely used in aerosol retrievals, has also been proven to describe a realistic empirical aerosol model well [26,27].

Broad band measurements in NIR/SWIR, which are always used for aerosol remote sensing, contain limited independent information on aerosol parameters for several reasons. Fundamentally, aerosol parameters have no specific spectral structure that could be easily characterized from the measured spectrum of interference of several gas absorption lines, e.g., CO_2 and H_2O. The continual scattering of aerosols in a broad band shows a similar effect to surface reflectance, especially multiple scatterings between aerosols and the surface and is the main issue in satellite remote sensing of aerosols. However, hyperspectral measurements that describes the lines in NIR/SWIR are different. Some studies have estimated aerosol information content from simulated GOSAT measurements, indicating that hyperspectral measurements can support part of the aerosol parameters retrieval independently [28]. The spectrum in the O_2-A absorption band could also be used in aerosol height retrieval [29]. However, when considering CO_2 retrieval together with aerosols, the aerosol model should be simplified. A Gamma distribution aerosol model with the three parameters shows positive evidence of the correcting aerosol effect when the 550 nm AOD is lower than 0.3 [24]. In the TanSat IAPCAS retrieval algorithm, we assume that the wavenumber dependence of aerosol extinctions with a bimodal lognormal distribution is quadratic in the retrieval of the coefficients [30,31].

Questions regarding the amount of aerosol parameter information that can be extracted and used for correction, as well as the determination of which aerosol parameters are most suitable for corrections, have been largely overlooked. The purpose of this study is to optimize the aerosol model used in the CO_2 retrieval algorithm to minimize aerosol-induced XCO_2 retrieval errors, using TanSat as an example and applying an information content estimation and error analysis based on the optimal estimation theory. The a posteriori errors of XCO_2 can be derived without any real retrieval process and can be used as the criteria for choosing an optimal aerosol model from simulated TanSat measurements.

In Section 2, the theoretical basis of the optimal estimation theory and the method used to quantify the information content and retrieval errors of CO_2 and aerosols are described. The numerical simulation of the TanSat spectrum and the assumptions necessary for the analysis are introduced in Section 3. In Section 4, we focus on estimating the information of the aerosol model in CO_2 retrieval, including the degree of freedom for signal (DFS) and interference in XCO_2. Changes in the CO_2

information and the impact of aerosols on XCO_2 retrieval errors for different aerosol models are evaluated in Section 5. Based on these analyses, the aerosol property combination groups appropriate for the synchronous retrieval of CO_2 are selected, and the aerosol-induced XCO_2 errors are minimized, while large amounts of CO_2 information remain available. The discussions about several limits and more scenarios of this study are shown in Section 7. Finally, the concluding section summarizes the new approach and explores the possible applications of this approach to future CO_2 retrievals.

2. Methodology

This research is underpinned by Rodgers' optimal estimation theory [32]. The **x** is used as the state vector consisting of *n* elements (such as the CO_2 profile) to be retrieved from an observation vector **y**, which contains *m* measurements (such as the hyperspectrum of the CO_2 band); then, **y** and **x** can be related as follows:

$$\mathbf{y} = \mathbf{F}(\mathbf{x}) + \varepsilon \tag{1}$$

where the forward model **F** describes the physical processes that link the measurements to the atmospheric components. ε represents the errors from both the observation process and the forward model. The purpose of retrieval is to resolve the state vector **x** from the satellite measurement vector **y**. The retrieved state vector $\hat{\mathbf{x}}$ with the maximum the *a posteriori* probability can be obtained by making the simulations (F(**x**)) closer and closer to the measurements (**y**) in iteration loops based on Bayes' theorem. This full physical inversion algorithm has been applied to various greenhouse gas and aerosol retrievals, both from space and the ground [5,18,30,33]. In this study instead of conducting any real retrieval process, such as simulation retrieval, we simply apply information content and linear error analysis, which was introduced by Rodgers [32].

2.1. Optimal Estimation Theory

Following the definition provided by [32], $\mathbf{S}_a$ is the error covariance matrix for the *a priori* state vector, $\mathbf{x}_a$, $\mathbf{S}_\varepsilon$ is the measurement error covariance matrix, and **K** is the weighting function matrix or Jacobian matrix, comprised of the partial derivative of each forward model output with respect to each retrieved parameter, i.e., $K_{i,j} = \partial F_i / \partial x_j$ (where $K_{i,j}$ represents the element in the *i*th row and the *j*th column in matrix **K**, F_i is the *i*th simulated measurement, and x_j is the *j*th element of the vector *x*). The Jacobians identify the sensitivity of observations to the retrieved parameters. The sensitivity of the retrieved state to the true state may be described by the averaging kernel matrix **A**, which is provided by the gain function $\mathbf{G}_y$:

$$\mathrm{A} = \frac{\partial \hat{\mathrm{x}}}{\partial \mathrm{x}} = \mathrm{G_y K}. \tag{2}$$

Given $\mathbf{S}_a$, $\mathbf{S}_\varepsilon$ and **K**, the gain function $\mathbf{G}_y$ is specified as follows:

$$\mathbf{G}_y = \left(\mathbf{K}^T \mathbf{S}_\varepsilon^{-1} \mathbf{K} + \mathbf{S}_a^{-1}\right)^{-1} \mathbf{K}^T \mathbf{S}_\varepsilon^{-1}. \tag{3}$$

The trace of the matrix **A** represents the DFS (i.e., the number of independent pieces of information yielded by the measurements). The closer **A** is to the identity matrix, the closer to perfect a retrieval will be, which means that the retrieved state changes completely with the true state without any interference. The averaging kernel matrix or DFS has been used to study the information content of the retrieved elements for trace gases or aerosol remote sensing [33–39]. After assessing the averaging kernel matrix **A** based on the *a priori* and measure error assumptions, the elements in **x** with greater information, which could be better retrieved from satellite observations, are decided without the retrieval process. In this study, the traces of the elements in matrix **A** corresponding to the CO_2 profile and aerosol parameters are called CO_2 DFS and aerosol DFS, respectively. In addition to the information of each retrieved element, all the a posteriori error components from different sources could be estimated by this method, as described in the following subsection.

2.2. Linear Error Analysis

For XCO_2 retrieval, the state vector **x** consists of the CO_2 profile $\boldsymbol{u}$ and non-CO_2 elements $\boldsymbol{e}$, including the surface reflectance, water vapor, surface pressure and aerosol properties, which are retrieved simultaneously:

$$\mathrm{x} = \begin{pmatrix} \mathrm{u} \\ \mathrm{e} \end{pmatrix}. \quad (4)$$

XCO_2 is defined as the retrieved CO_2 profile weighted by the pressure weighting function $\boldsymbol{h}$, such that $XCO_2 = h^T\hat{\mathbf{x}}$. In fact, those elements of $\boldsymbol{h}$ corresponding to the non-CO_2 profile (ê) are zero. As shown in [16,17], the a posteriori error of XCO_2 results from a list of sources, including the *a priori* uncertainties of the CO_2 profile, interference of the non-CO_2 retrieved parameters, and inaccurate observation processes. Thus, the uncertainty in XCO_2 is expressed as follows:

$$\Delta X_{CO2} = \mathbf{h}^T(\hat{\mathbf{x}} - \mathbf{x}) = \mathbf{h}^T(\mathbf{A}_{uu} - \mathbf{I})(\mathbf{u} - \mathbf{u}_a) + \mathbf{h}^T\mathbf{A}_{ue}(\mathbf{e} - \mathbf{e}_a) + \varepsilon_u. \quad (5)$$

Here, $\mathbf{A}_{\mathrm{uu}}$ and $\mathbf{A}_{\mathrm{ue}}$ are submatrices of **A**, denoting the CO_2-only components, and components characterized by the relationship between the CO_2 profile $\boldsymbol{u}$ and non-CO_2 elements $\boldsymbol{e}$, respectively. **I** is the identity matrix, and the subscript a represents the *a priori* uncertainty. The first term on the righthand side of Equation (5) is the smoothing error derived from the CO_2 profile uncertainty, and the second term represents the interference error caused by non-CO_2 components in the state vector. ε_u includes all other errors. The corresponding covariance matrix for each error source can be specified as follows. The smoothing error covariance matrix is as follows:

$$\hat{\mathbf{S}}_s = (\mathbf{A} - \mathbf{I})\mathbf{S}_{\mathrm{a}}(\mathbf{A} - \mathbf{I})^T. \quad (6)$$

The interference error is calculated using the following:

$$\hat{\mathbf{S}}_i = \mathbf{A}_{ue}\mathbf{S}_{\mathrm{ec}}\mathbf{A}_{ue}{}^T, \quad (7)$$

where $\mathbf{S}_{\mathrm{ec}}$ describes the ensemble covariance for the non-CO_2 elements, which is not necessarily equal to the *a priori* error, $\mathbf{S}_{\mathrm{a}}$. If considering the error in XCO_2 due to each state vector element (σ_{XCO2e}), the expression is as follows:

$$\sigma_{XCO2e,j} = \begin{cases} \boldsymbol{h}^T(\mathbf{A} - \mathbf{I})\sigma_j, j = 1,\ q \\ \boldsymbol{h}^T\mathbf{A}\sigma_j, j = q+1,\ n \end{cases}, \quad (8)$$

where σ_j is the *a priori* uncertainty (or the square root of $\mathbf{S}_{\mathrm{ec}}$ for non-CO_2 elements) of each state vector element. The first q elements represent uncertainties related to the CO_2 profile (i.e., the smoothing errors) while the others are the interference error components.

Two further errors include measurement noise and the forward model parameter uncertainties, which are not retrieved in the state vector. For measurement errors, the covariance matrix $\hat{\mathbf{S}}_m$ is described by the following:

$$\hat{\mathbf{S}}_m = \mathbf{G}_y\mathbf{S}_\varepsilon\mathbf{G}_y^T, \quad (9)$$

where $\mathbf{S}_\varepsilon$ is an estimation of the actual measurement errors. In our study, we only considered the measurement noise based on the instrument signal-to-noise ratio (SNR) and the simulated spectra of TanSat. Based on the errors of the forward model parameter $\mathbf{S}_{\mathrm{b}}$ and the Jacobians with respect to parameter $\mathbf{K}_{\mathrm{b}}$, we specified the forward model parameter error covariance as follows:

$$\hat{\mathbf{S}}_f = \mathbf{G}_y\mathbf{K}_{\mathrm{b}}\mathbf{S}_{\mathrm{b}}\mathbf{K}_{\mathrm{b}}^T\mathbf{G}_y^T. \quad (10)$$

In fact, in some studies, the a posteriori error only includes the first three errors noted above. The forward model and all the parameter inputs are as accurate as they can be; otherwise, we could improve the forward model. However, for our research regarding aerosol effects, if all the parameters in the aerosol model are not retrieved with CO_2, the uncertainties of those nonretrieved parameters should be considered in the XCO_2 retrieval error. Thus, the forward model parameter error related to the nonretrieved aerosol parameter uncertainties is also included in our analysis. The errors in other aerosol parameters, retrieved synchronously with CO_2, are components of the interference error. Finally, the total covariance matrix is the sum of each component:

$$\hat{\mathbf{S}} = \hat{\mathbf{S}}_s + \hat{\mathbf{S}}_i + \hat{\mathbf{S}}_m + \hat{\mathbf{S}}_f. \tag{11}$$

The a posteriori error variance in XCO_2 is $\sigma^2_{XCO2} = h^T\hat{\mathbf{S}}h$, and the corresponding error variance due to each error source can also be calculated in the same way by replacing $\hat{\mathbf{S}}$ with another covariance matrix, such as the XCO_2 interference error σ_i, which is estimated by $\sigma_i^2 = h^T\hat{\mathbf{S}}_i h$. In other words, the XCO_2 a posteriori error σ_{XCO2} is the sum of σ_s, σ_i, σ_m and σ_f. Generally, when focusing on the XCO_2 error due to aerosol parameters, those components related to aerosol parameters, both in the interference error and the forward model parameter error, are evaluated and compared among different aerosol models.

From the hyperspectra and Jacobians in the O_2-A band, and two CO_2 NIR absorption bands of the TanSat, which is simulated by a vector linearized discrete ordinate radiative transfer model (VLIDORT), the DFS values of both CO_2 and aerosol properties in the state vector are calculated. After quantifying 4 components of the XCO_2 retrieval errors, errors related to aerosol parameter uncertainties were brought into focus. When the aerosol model in the CO_2 retrieval algorithm is altered, the corresponding DFS and retrieval errors differ, particularly those associated with aerosol properties. Accordingly, we sought to identify the ensemble of aerosol parameters in the aerosol model that yielded the largest amount of CO_2 information with the fewest aerosol-induced XCO_2 errors. Considering the complex aerosol mixtures, four aerosol scenarios were compared according to different solar zenith angles (SZAs). In adopting this new approach, the aerosol model is optimized to minimize the interference of aerosols in XCO_2 retrieval and could be applied to future retrievals from real data.

3. TanSat Simulations and Retrieval Assumptions

The application of the theory introduced in the preceding section initially requires measurement and state vector definitions, as well as the error covariance matrices. Based on the characteristics of the ACGS onboard TanSat, we used a forward model to simulate the ACGS spectra in three NIR bands and their Jacobians with respect to each element in the state vector. For the TanSat, there are three observation modes with different goals: nadir mode viewing nadir target, which is used for over-land observations; sun-glint mode, which looks at the sun glint to obtain more reflected radiance over the water body with low surface reflectance; and target mode, which is aimed at single point observations with different angles. In this research, we only focus on CO_2 retrieval in nadir mode over land, so the satellite viewing zenith angle (VZA) is maintained at 0° (nadir), and the scattering angle varies from only several SZAs. In this section, we briefly describe the instrument characteristics and the forward model, particularly the details of the aerosol models. Subsequently, the necessary assumptions regarding the *a priori* and measurement error covariance matrices are presented.

3.1. Simulation Input

The forward model used to simulate the TanSat observations consisted of a linearized single-scattering code for spherical particles, a radiative transfer model called VLIDORT that can compute analytical weighting functions [40], and a surface model calculating bidirectional reflectance distribution function (BRDF), as well as modules computing the molecular Rayleigh scattering and trace gas absorption. A similar model was used in the GOSAT and TanSat CO_2 retrieval algorithms [5,30,41]. Before conducting a simulation using the forward model, some necessary inputs related to the instrument characteristics, atmospheric states, surface and aerosol types, and observation geometry must be understood. After inputting these parameters, the Stokes vector and their Jacobians with respect to each retrieved parameter (K_{ij}), were computed, based on the radiative transfer equation from the forward model.

For the TanSat, the hyperspectral instrument ACGS measures spectra in three bands: the O_2-A band, the CO_2 weak absorption band, and the strong NIR absorption band (hereafter expressed as the 1CO_2 and 2CO_2 bands). The key characteristics of ACGS are presented in Table 1. The spectral resolution defined by the full width at half maximum (FWHM) and an instrument model are necessary for simulating the spectrum detected by the instrument. After the line-by-line radiative transfer calculations are completed, the original spectrum is convoluted by a Gaussian instrument line shape described by FWHM. The atmospheric temperature, pressure, water vapor and trace gases profiles originate from the US standard atmosphere profile of AFGL (1980). The CO_2 profile is scaled by a factor based on the near real-time CO_2 data from the global CarbonTracker model [42], which also serves as the *a priori* profile.

Table 1. Characteristics of Atmospheric Carbon Dioxide Grating Spectrometer (ACGS) on board the TanSat.

Instrument Characteristics	Value		
Band name or number	O_2-A	CO_2 weak	CO_2 strong
Spectral range (nm)	758–778	1594–1624	2041–2081
Center wavelength (nm)	768	1610	2060
FWHM (nm) [1]	0.04	0.12	0.16
SNR [1]	360	250	180
Spatial resolution (km)		1×2	
Scan range (o)		−30~10	
Swath (km)		20	

[1] SNR, signal-to-noise ratio; FWHM, full width at half-maximum.

For surface reflectance, we selected the BRDF model of the Moderate Resolution Imaging Spectroradiometer (MODIS) [43,44] for typical land surfaces, including vegetation and bare soil, instead of Lambertian albedo without angular dependence. As shown in previous studies [45], most land surfaces could be regarded by a fraction as a linear combination of vegetation and soil. Therefore, we believe the experiments over these two surface types are adequate for our research over land. The three Ross-Li kernels in the MODIS BRDF describe the isotropic, volumetric, and geometric-optical surface scatterings [46,47]. For our study, we selected one grid from the MODIS observations of vegetation or soil as an example. The coefficients of each kernel were derived from MODIS products and extrapolated to the center wavelength of each ACGS band, on the assumption that surface reflectance underwent little change in each band (Table 2), which is similar to the CAPI research that we have previously conducted [20]. The corresponding surface reflectivities implied by the BRDF model evaluated in the direct beam, sun-surface-satellite geometries are shown in the Supplemental Material (Figure S5).

Table 2. Bidirectional reflectance distribution function (BRDF) coefficients of three kernels in each ACGS band defined for both soil and vegetation.

Center Wavelength (nm)	$f_{iso}(\lambda)$ [1]	$k_1(\lambda)$ [1]	$k_2(\lambda)$ [1]
768	0.8632/0.2525 [2]	0.1747/0.1650	0.2569/0.0226
1610	0.2107/0.4197	0.1100/0.1670	0.0286/0.0550
2060	0.1052/0.3279	0.0305/0.0826	0.0236/0.0670

[1] $f_{iso}(\lambda)$, $k_1(\lambda)$ and $k_2(\lambda)$ represent amplitude factors for the Lambertian, Ross-thick and Li-sparse kernels, respectively. Details of the BRDF equation may be found in Equation (12) in [20]. [2] The value left of the symbol "/" is for vegetation surface and the right value is for soil

In the simulations, aerosol particles were assumed to be spherical with a bimodal lognormal particle size distribution (PSD) function, characterized by effective radius r_{eff} and effective variance v_{eff} for both fine and coarse modes [34,48,49]. To describe aerosol composition, the complex refractive indices for both aerosol modes are required in addition to the PSD parameters. A Gaussian shape is assumed for the aerosol extinction profile, which is described by peak height and width at the aerosol extinction half maximum [39,50]. Because human activities near the surface are the main sources of heavy haze or air pollution and under these circumstances CO_2 retrieval is significantly affected, our focus in this study is on tropospheric aerosols with low peak heights. Although stratospheric aerosols could also result in CO_2 retrieval uncertainties, as OCO-2 studies have shown [19], most are related to less frequent volcanic eruption or smaller AODs.

Considering the various emission sources and mixtures of aerosol particles that exist, several typical aerosol types with different microphysical properties were simulated and compared. Based on work by Dubovik [51], multiyear, global data from the Aerosol Robotic Network (AERONET) of ground-based observations were used to represent distinct aerosol optical properties at key locations. Daily averaged inversion products from the last five years at similar AERONET sites used by Dubovik [51] were included to obtain the representative properties for four main aerosol types: urban–industrial (UI), biomass burning (BB), desert dust (DD) and marine aerosols (MA). According to the accuracy of individual AERONET retrievals, a decrease in aerosol information content for low aerosol loading could result in significant uncertainties in refractive index retrievals. Therefore, only those products with AOD at 440 nm (AOD_{440}) larger than 0.4 for UI and BB aerosols, AOD at 1,020 nm (AOD_{1020}) larger than 0.3, and an Ångström exponent (between 440 and 870 nm) smaller than 0.6 for DD are involved in our analysis, similar to the AERONET products quality document. The variability of the screened aerosol column volume concentration (V^f and V^c), $r_{eff}{}^f$ and $r_{eff}{}^c$, and $v_{eff}{}^f$ and $v_{eff}{}^c$, for fine and coarse particles at the center wavelength are presented in Figure 1. Figure 2 shows the histograms of fitted m_r and m_i, assuming little variation in each band. In addition to the V^f and V^c, and $r_{eff}{}^f$ and $r_{eff}{}^c$ of the UI and BB aerosols, other parameters exhibit little relationship with the AOD. Consequently, the statistics of the aerosol properties, expressed as means ± standard deviation, or as a linear relationship with AOD, are presented in Table 3, which is similar to Table 1 in the study by Dubovik [51]. Considering the AOD range for each aerosol type, we assumed 1.0 AOD_{440} for UI and BB aerosols, 0.7 AOD_{1020} for DD, and 0.15 AOD_{1020} for MA in our simulations, and we input the corresponding microphysical parameters using the relationships presented in Table 3. Aside from the microphysical properties, an aerosol extinction profile with a 2-km peak height was assumed for all aerosol types, indicating aerosol concentrations at the top of the boundary layer.

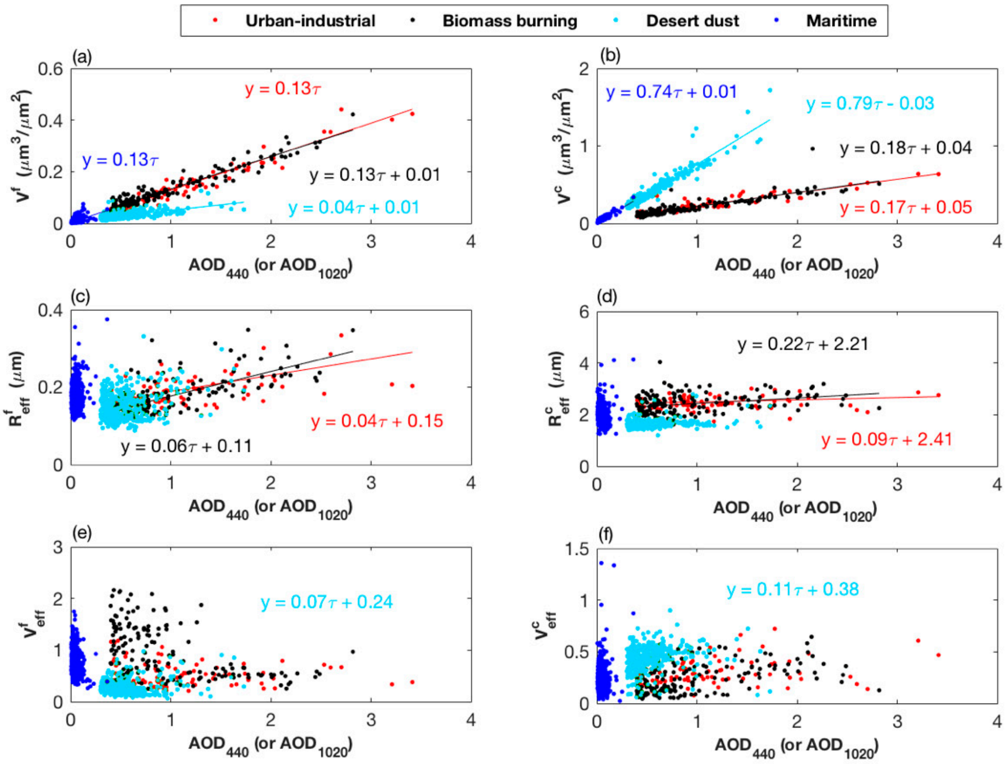

Figure 1. The scatter plot of aerosol column volume concentration (V^f and V^c), effective radius ($r_{eff}{}^f$ and $r_{eff}{}^c$) and effective variance ($v_{eff}{}^f$ and $v_{eff}{}^c$) for fine and coarse particles. The x-axis represents aerosol optical depth (AOD) at 440 nm for urban–industrial (UI) and biomass burning (BB) aerosols and AOD at 1020 nm for desert dust (DD) and marine aerosols (MA) aerosols. The red, black, light blue and blue points (lines, equations) are data for UI, BB, DD and MA, respectively. The straight lines are the results of linear fitting described by the equations in the plots.

The model primarily simulates TanSat nadir viewing observations with a 0° relative azimuth angle. To compare the dependence on the scattering angle, cases with SZAs from 20° to 65° were simulated. The corresponding Jacobians with respect to all parameters in the bimodal aerosol model were also output and presented in Figure 3. The distinct patterns of the various aerosol parameters illustrate the sensitivities of the ACGS measurements to the aerosol properties, which indicateds that some aerosol properties are independent and their information may be obtained through observations. The correlation coefficient matrix of these aerosol parameters is calculated from the posteriori error covariance matrix, as shown in Figure S5 in the Supplement. The high correlations between several parameters lead to their similar information content. The Jacobians of surface BRDF coefficients are also shown in the Supplement and not analyzed here.

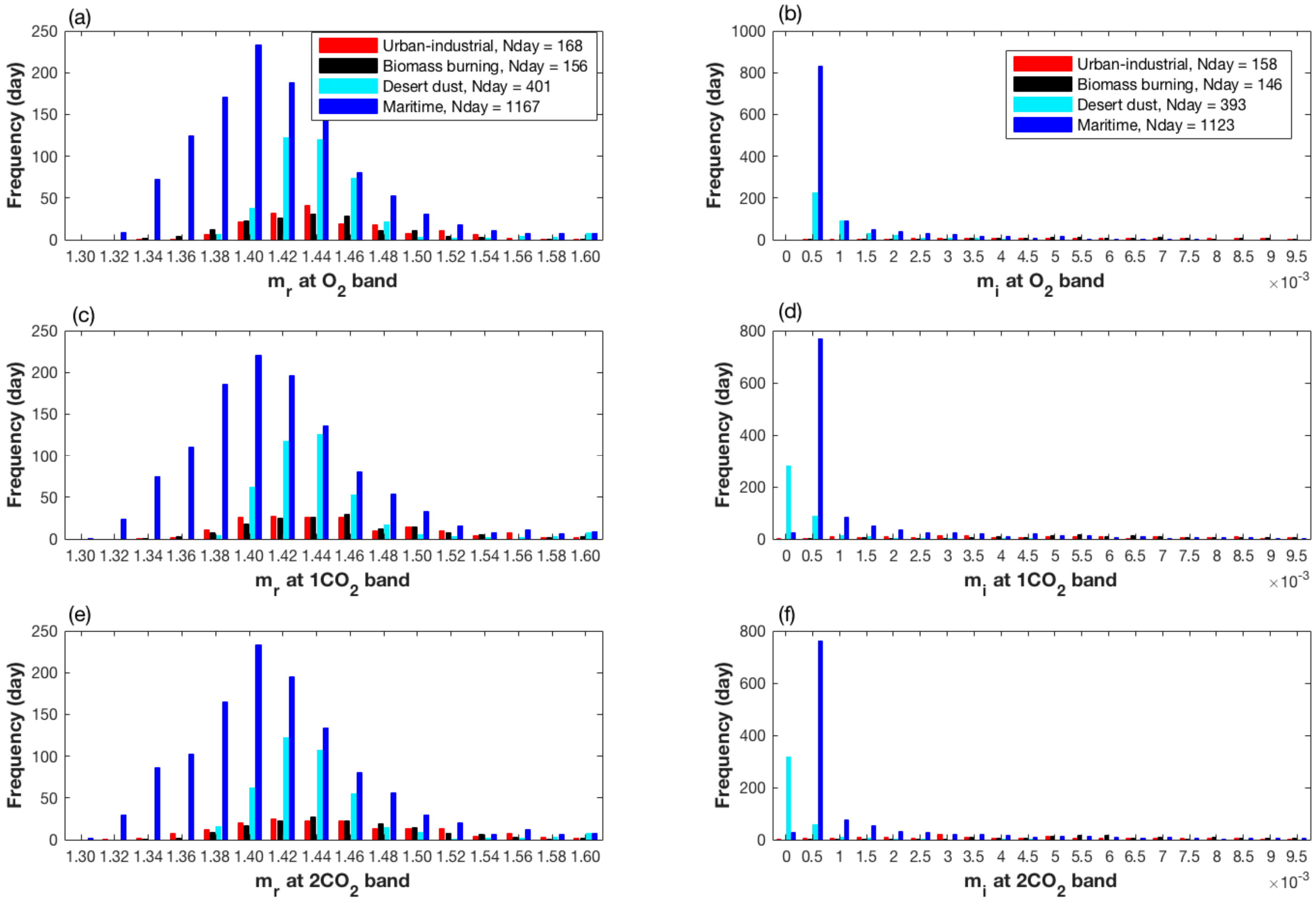

Figure 2. The histograms of m_r (**a**,**c**,**e**) and m_i (**b**,**d**,**f**) in three ACGS bands fitted by Equations (12) and (13). The m_r and m_i are assumed do not change with the wavelength in each band. Four colorful bars represent four aerosol types as in Figure 2.

Table 3. Summary of the aerosol optical properties for both fine and coarse modes based on the inversion products of the selected Aerosol Robotic Network (AERONET) sites [1].

Aerosol Type	Urban–Industrial	Biomass Burning	Desert Dust	Marine Aerosol
AERONET site	Beijing_RADI (China)	Alta Floresta (Brazil)	Capo Verde (Capo Verde)	Lanai (Hawaii, USA)
Time and number of measurements (total)	2012–2017 (Jun–Sep) 306 (1119) [2]	2011–2016 (Aug–Oct) 163 (374) [2]	2012–2017 1012 (1012) [2]	1998–2004 1167 (1167) [2]
Number of measurements (chosen) [3]	168	156	401	1167
AOD range	$0.4 \leq$ AOD440 ≤ 3.4	$0.4 \leq$ AOD440 ≤ 2.8	$0.3 \leq$ AOD1020 ≤ 1.7	$0.007 \leq$ AOD1020 ≤ 0.37
m_r [4]	1.459 ± 0.04/1.461 ± 0.05/1.461 ± 0.06	1.450 ± 0.04/1.462 ± 0.05/1.466 ± 0.05	1.452 ± 0.04/1.448 ± 0.04/1.446 ± 0.04	1.42 ± 0.05
m_i [4]	0.0081 ± 0.015 /0.0059 ± 0.015/0.0052 ± 0.015	0.0078 ± 0.015/0.0069 ± 0.015/0.0066 ± 0.015	0.0009 ± 0.003/0.0003 ± 0.011/0.0002 ± 0.016	0.0005 ± 0.008
r_{eff}^f (μm)/v_{eff}^f	y = 0.04AOD440 + 0.15 ± 0.04/0.57 ± 0.24	y = 0.06AOD440 + 0.11 ± 0.035/0.96 ± 0.52	0.15 ± 0.04/y = 0.07AOD1020 + 0.24 ± 0.14	0.16 ± 0.03/0.75 ± 0.19
r_{eff}^c (μm)/v_{eff}^c	y = 0.09AOD440 + 2.41 ± 0.30/0.32 ± 0.12	y = 0.22AOD440 + 2.21 ± 0.38/0.24 ± 0.14	1.64 ± 0.16/y = 0.11AOD1020 + 0.38 ± 0.12	1.99 ± 0.26/0.20 ± 0.10
V^f (μm^3/μm^2)	y = 0.13AOD440 ± 0.02	y = 0.13AOD440 + 0.01 ± 0.02	y = 0.04AOD1020 + 0.01 ± 0.01	y = 0.13AOD1020 ± 0.007
V^c (μm^3/μm^2)	y = 0.17AOD440 + 0.05 ± 0.06	y = 0.18AOD440 + 0.04 ± 0.06	y = 0.79AOD1020 − 0.03 ± 0.055	y = 0.74AOD1020 + 0.01 ± 0.009

[1] Most values are accompanied by a standard deviation following the symbol "±". The superscript f represents the parameter for fine mode and c represents that for coarse mode. [2] The numbers in brackets are the total numbers in the whole year, and those outside were collected over several months, following Dubovik [46]. [3] The numbers are those following filtering to guarantee the accuracy of aerosol refractive index retrieval, using the criteria referenced in the main text. [4] The m_r and m_i are at 768 nm, 1610 nm and 2060 nm, respectively, fitted by the products at four observed AERONET wavelengths, based on Equations (12) and (13).

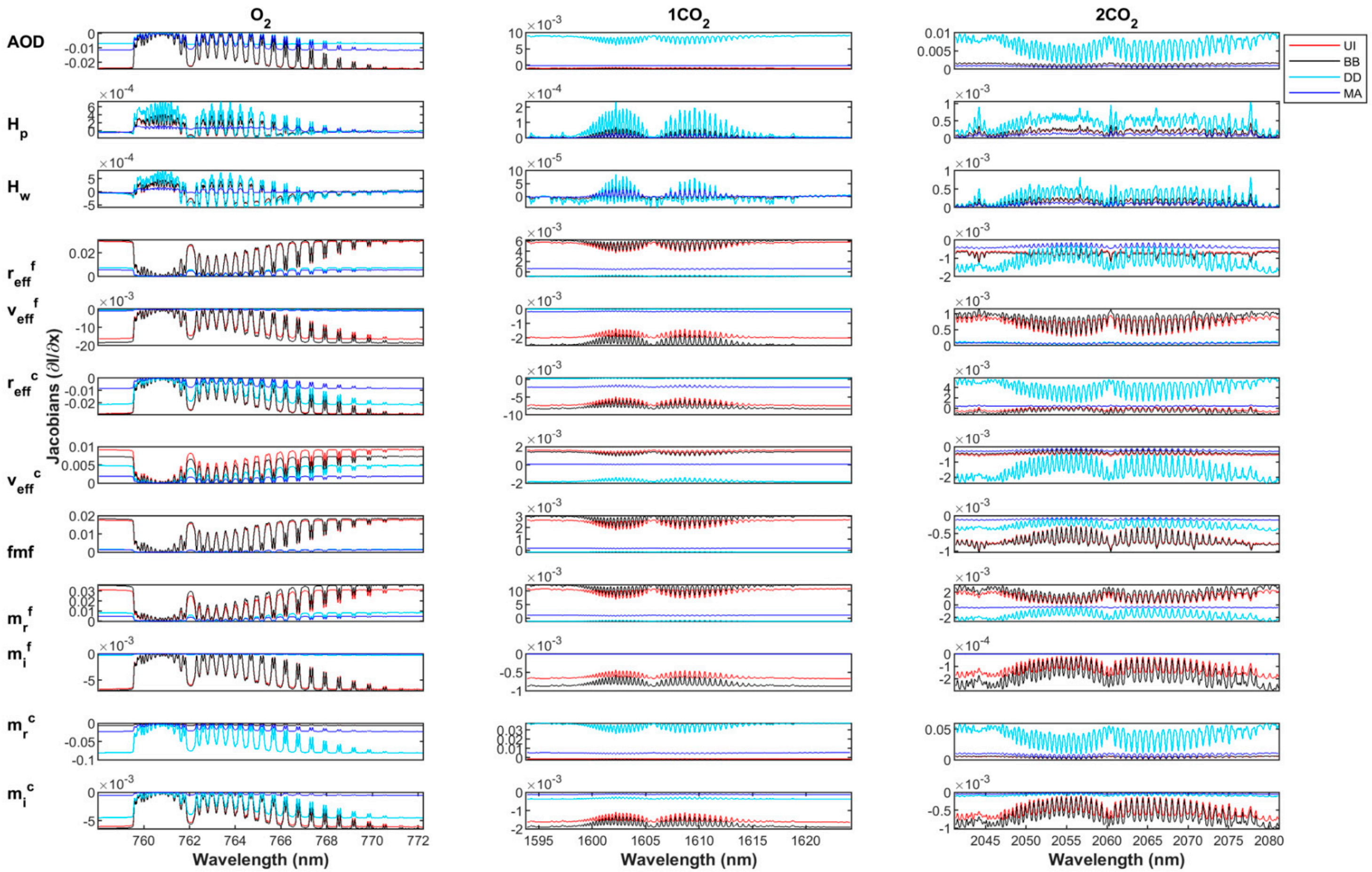

Figure 3. The simulated weighting functions of each aerosol parameter at three ACGS bands. The rows from top to bottom represent different aerosol parameters: AOD, peak height of aerosol profile (H_p), width of aerosol profile (H_w), effective radius for fine particles (r_{eff}^f), effective variance for fine particles (v_{eff}^f), effective radius for coarse particles (r_{eff}^c), effective variance for coarse particles (v_{eff}^c), fine mode fraction (fmf), real part of refractive index for fine particles (m_r^f), imaginary part of refractive index for fine particles (m_i^f), real part of refractive index for coarse particles (m_r^c), and imaginary part of refractive index for coarse particles (m_i^c). Three columns from left to right show different bands: O_2 A band, 1.6 µm CO_2 absorption band ($1CO_2$) and 2.06 µm CO_2 absorption band ($2CO_2$). Four colors represent four types of aerosols: UI, BB, DD and MA.

3.2. The State Vector Defination

The state vector $\boldsymbol{x}$ for CO_2 retrieval consists of the CO_2 mixing ratio profile ($\boldsymbol{u}$) and non-CO_2 elements ($\boldsymbol{e}$), including the H_2O scaling factor, surface pressure, aerosol parameters, and surface BRDF factors. The H_2O mixing ratio profile is scaled by a factor to describe the variation in the H_2O column amount while ignoring changes in profile shape, as in Chen, Yang, Cai, Liu and Spurr [21]. Table 4 summarizes all possible elements included in the state vector, where the aerosol parameters were composed of the 14 parameters used in our previous analysis [20] and two further aerosol profile parameters. In fact, for different aerosol models, different parts of these aerosol parameters are chosen for the state vector, while the remainder serve as the forward model parameters.

Table 4. The state vector for TanSat CO_2 retrieval and the corresponding *a priori* uncertainty.

	Parameter	Number of Parameters	*a priori* Uncertainty (1σ)
CO_2 (ppm)	Mixing ratio profile	15	(21.28, 16.7, 13.3, 9.86, 8.0, 7.09, 6.5, 6.0, 5.53, 4.79, 3.87, 2.75, 1.96, 1.84, 3.72)
H_2O (ppm)	Scaling factor of mixing ratio profile	1	50%
Surface pressure (hPa)	Pressure at surface layer	1	1%
Aerosol	Aerosol optical depth (AOD)	1	100%
	The effective radius (r_{eff}) of particle size distribution (PSD) for each mode	1 × 2	From AERONET
	The effective variance (v_{eff}) of PSD for each mode	1 × 2	From AERONET
	The peak height of aerosol profile (H_p)	1	100%
	The half width of aerosol profile (H_w)	1	100%
	Fine mode fraction (fmf)	1	100%
	Parameters for real part of refractive index for each mode (a_r, b_r) [1]	2 × 2	From AERONET
	Parameters for imaginary part of refractive index for each mode (a_i, b_i) [1]	2 × 2	From AERONET
Surface	BRDF coefficient of Lambertian kernel in each band	1 × 3	20%

[1] a_r, b_r, a_i and b_i correspond to those parameters in Equations (12) and (13).

As is consistent with previous analyses, the wavelength dependence of the real and imaginary parts of the refractive index (m_r, m_i) are also assumed to be exponent functions, following Dubovik and King [52]:

$$m_r(\lambda) = a_r * \lambda^{b_r}, \tag{12}$$

$$m_i(\lambda) = a_i * \lambda^{b_i}. \tag{13}$$

where the a_r, b_r, a_i and b_i values are the fitting coefficients and were included in the state vector. The derivations of the Jacobians were presented in a previous study [53]. The Jacobians of these coefficients, rather than the Jacobians of the refractive index, were involved in CO_2 retrieval.

3.3. The A Priori and Measurement Error Assumptions

In addition to the simulated spectra, error analysis requires characterization of the *a priori* error covariance matrix $\mathbf{S}_a$ and the measurement error covariance matrix $\mathbf{S}_\epsilon$. The *a priori* uncertainty of each retrieved parameter, described as a standard deviation (1σ), is summarized in Table 4. To prevent any unreasonable perturbation of the retrieved CO_2 profile, we imposed smoothness constraints on the CO_2 profile via nonzero off-diagonal elements in the *a priori* error covariance matrix, $\mathbf{S}_{a_{CO2}}$. The square roots of the diagonal elements of $\mathbf{S}_{a_{CO2}}$ from the surface to the top of atmosphere (TOA) are presented in Table 4 and expressed as a vector $\boldsymbol{\sigma}_{aCO2}$. Figure 4 presents the correlation coefficient matrix ($\mathbf{R}$) of the CO_2 concentrations in 15 layers, similar to [18]. In other words, $\mathbf{S}_{a_{CO2}}$ is calculated by $\mathbf{R}\boldsymbol{\sigma}_{aCO2}\boldsymbol{\sigma}_{aCO2}^T$. Overall, the total *a priori* uncertainty of XCO_2 is scaled to approximately 5.6 ppm. The *a priori* error of water vapor column concentration is assumed to be 50% to describe its large uncertainty. The higher accuracy of the surface pressure results in a smaller uncertainty. While the *a priori* uncertainties of AOD, aerosol profile parameters, and fine mode fraction (fmf) (100%) for different aerosol types were assumed to be equivalent, and the standard deviation of the inversion products from four AERONET sites (Table 4) were used as the *a priori* uncertainties of the refractive index coefficients (a_r, b_r, a_i and b_i) and PSD parameters (r_{eff} and v_{eff}). Considering the crucial role of the Lambertian kernel in the three-kernel BRDF surface model, we only retrieved the BRDF coefficient for the Lambertian kernel at each band, and the *a priori* uncertainty was assumed to be 20%. Further analysis of the influences of different surface reflectances on aerosol interference are shown in the Supplemental section and not presented in the main text. Similar to the assumptions in Dubovik, et al. [54], Xu and Wang [33] and Chen, Wang, Liu, Xu, Cai, Yang, Yan and Feng [20], we believe that the *a priori* errors for non-CO_2 retrieved parameters are independent from one another, so $\mathbf{S}_{a_{CO2}}$ is defined as a diagonal matrix. Combined with $\mathbf{S}_{a_{CO2}}$, which is defined in Table 4 and Figure 4, the total *a priori* error covariance matrix $\mathbf{S}_a$ may be expressed as follows:

$$\mathbf{S}_a = \begin{bmatrix} \mathbf{S}_{a_{CO2}} & 0 \\ 0 & \mathbf{S}_{a_{other}} \end{bmatrix}. \quad (14)$$

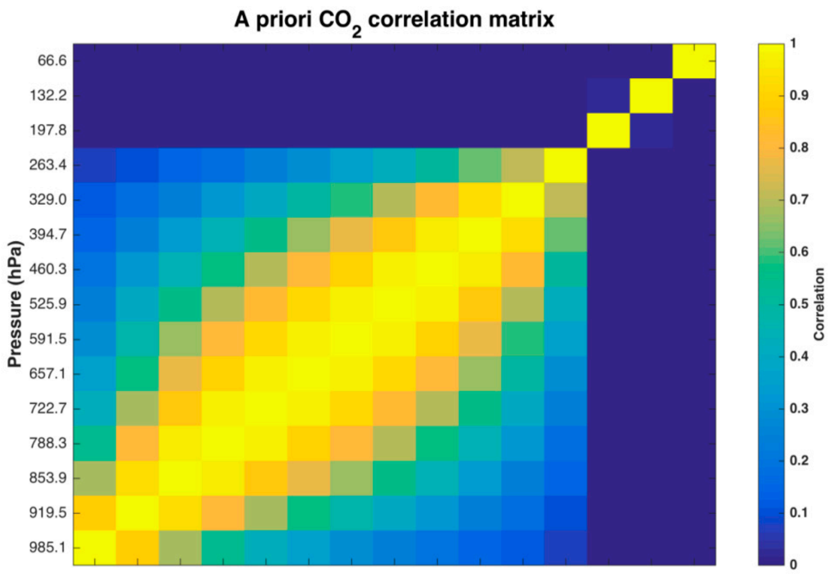

Figure 4. The a priori CO_2 correlation matrix. The colors represent the error correlation coefficients between CO_2 concentrations at different levels, and the pressures are presented on the left.

Because the calibration and systematic errors could be removed from the retrieval algorithm to some extent, only measurement noise was considered in this study, which is calculated by the spectra signal and corresponding SNR in each band as follows:

$$\text{Noise} = \frac{\text{Spectra}_{\text{ACGS}}}{\text{SNR}_{\text{ACGS}}}. \quad (15)$$

The corresponding SNR could be interpolated from the SNR curves provided by the experiments conducted in the laboratory (SNR curves for all bands are shown in the Supplement). Similarly, measurement noise was also assumed to be noncorrelated, so the error covariance matrix $\mathbf{S}_\varepsilon$ is a diagonal matrix with the square of noise as the diagonal elements.

4. Aerosol Parameters in CO_2 Retrieval

Based on the method detailed in Section 2 and the assumptions presented in Section 3, the information of aerosol parameters described as DFS and their resulting XCO_2 retrieval errors were calculated. In this section, we first include all 16 parameters of the aerosol model in the state vector of CO_2 retrieval, and therefore, the aerosol property uncertainties only resulted in interference errors rather than in forward model parameter errors for XCO_2. The interference errors caused by each aerosol parameter were estimated and compared. In addition to the XCO_2 error analysis, we also considered how many independent aerosol parameters may be retrieved simultaneously with CO_2. To address this question, the DFS of all aerosol parameters for the four aerosol types and different SZAs were calculated. As a result, the aerosol parameters with significant information from the TanSat observations were selected. This conclusion is also available concerning the aerosol model parameters that result in greater errors in the XCO_2 retrieval.

4.1. Aerosol-Induced XCO_2 Retrieval Errors

The interference errors in XCO_2 for each aerosol parameter of the four aerosol types (calculated by Equation (8)) are presented in Figure 5a. These errors from different aerosol parameters range from less than 0.1 to 0.8 ppm. Overall, the interference errors due to r_{eff} and v_{eff} for both fine and coarse modes, as well as fmf and a_r for fine mode, exceed those for the other parameters, reaching 0.2 ppm or more at 20° SZA. Because of the dominance of large particles, the coarse mode PSD parameters of DD result in larger uncertainties than the fine particle parameters, while the opposite is the case for UI and BB aerosols, where smaller particles predominate. Regarding the refractive index coefficients, their interference errors were less than 0.2 ppm at 20° SZA, and even less than 0.1 ppm for MA. These refractive index-related errors ranged from 0.1 to 0.2 ppm for DD aerosols, which was slightly more than for the other aerosol types. When the interference errors at different SZAs were compared, it was observed that at a smaller SZA, the errors from most aerosol parameters were larger. The reason for this is that more information is allocated to the CO_2 profile than to the aerosol properties for longer light paths at larger SZAs, so there is a reduction in the impact of the aerosol parameter uncertainties on XCO_2 retrieval (Equation (8)).

When the interference errors (σ_i) from all aerosol parameters are summed ($\sigma_i^2 = h^T \hat{\mathbf{S}}_i h$), the aerosols will induce a 0.2 to 1.0 ppm error in the XCO_2 retrievals, depending on the aerosol type and the observation geometry (Figure 5b). Comparison of the four aerosol types reveals that the UI, DD and BB aerosols have greater effects on XCO_2 retrieval due to their larger AODs, with an interference error of greater than 0.3 ppm. The MA only cause interference errors of 0.2 to 0.3 ppm, as MA has the lowest aerosol loading. When the SZA is increased, the interference of the aerosols with XCO_2 is weakened, except for MA, owing to the longer light paths. For DD, this pattern changes when the SZA is 65°, which is related to the scattering phase matrix. Furthermore, for a soil surface with a larger reflectance, the interference errors in XCO_2 caused by aerosol parameters are slightly smaller (Figure S2 in the Supplement), indicating that aerosol scattering has a larger impact due to a lower reflected radiation signal from the satellite.

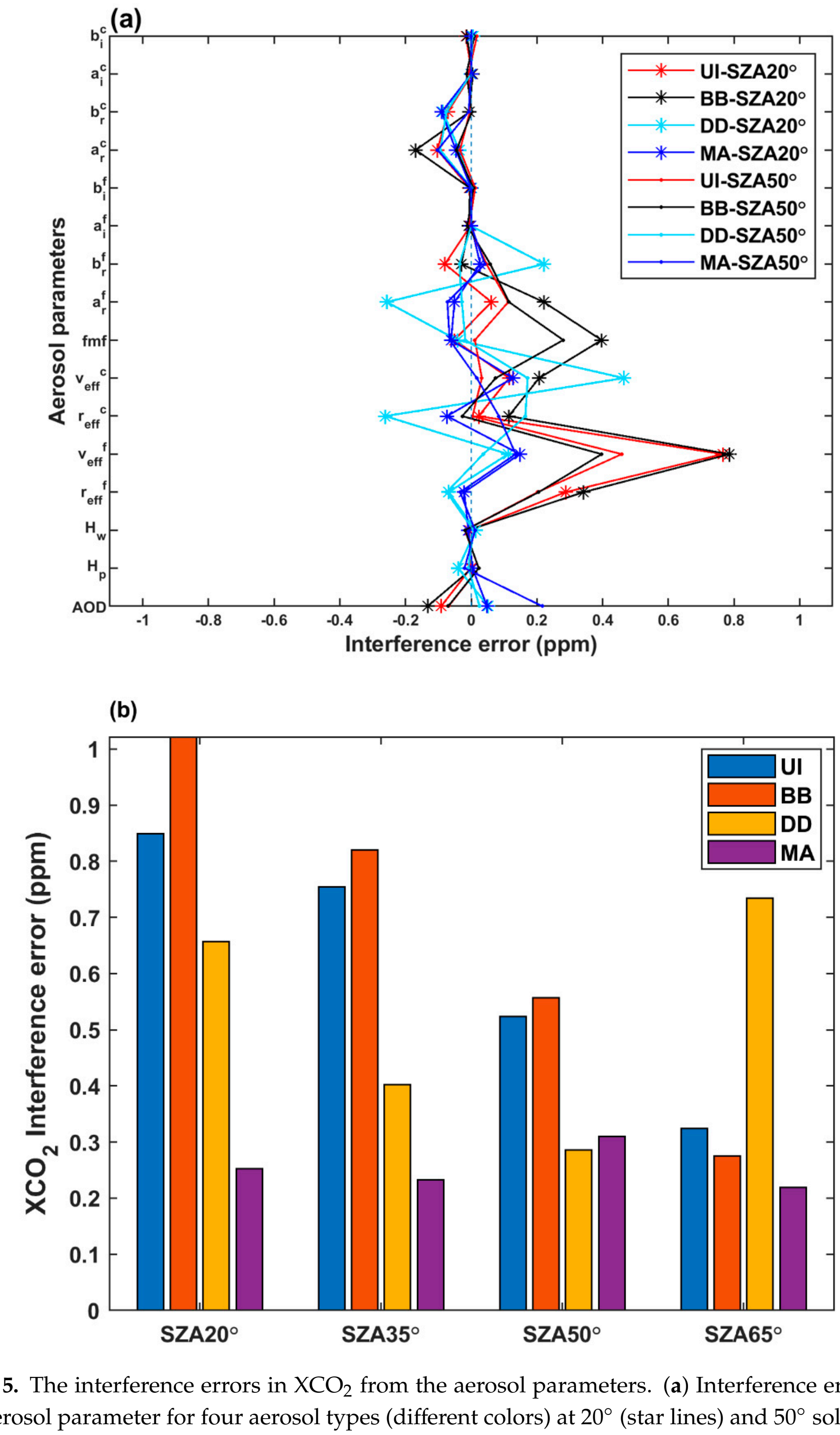

Figure 5. The interference errors in XCO_2 from the aerosol parameters. (**a**) Interference error from each aerosol parameter for four aerosol types (different colors) at 20° (star lines) and 50° solar zenith anlge (SZA) (dot lines) over vegetation. The x-axis is the interference error and the y-axis represents 16 aerosol parameters. (**b**) Total interference error from all aerosol parameters at four SZAs for different aerosol types over vegetation.

In summary, the aerosol parameter uncertainties constitute a significant component of XCO_2 retrieval uncertainty, depending on the aerosol type and observation geometry, or the scattering phase matrix in different scattering angles. This finding presents a challenge that must be overcome before XCO_2 retrieval precision can be improved.

4.2. Aerosol Information

Although all 16 aerosol parameters were included in the CO_2 retrieval for our analysis, it is possible that TanSat NIR hyperspectral measurements only contain sufficient information for certain aspects of these parameters. Therefore, we verify the DFS of each aerosol parameter in the CO_2 retrieval shown in Figure 6 to determine the parameters that could be retrieved simultaneously with CO_2. The total DFS of the aerosol parameters for the UI, BB, and DD is six to seven, indicating that around six or seven independent aerosol parameters may be retrieved together with CO_2. For MA, only four to five retrievable aerosol parameters exist. A comparison of the DFS among the aerosol parameters reveals that the DFSs of the AOD, H_p, and H_w (i.e., the first three) are large (mostly close to 1.0) for all aerosol types at any viewing geometry, while the information concerning the other parameters varies significantly according to aerosol type and observation geometry. In any case, it appears that AOD, H_p, and H_w can be retrieved from the ACGS hyperspectral observations. Additionally, the aerosol DFS over soil only has a 0.1–0.2 difference from that of a vegetation surface. There is almost no distinction in the decision of how much aerosol parameter information could be derived from satellite measurements over different surface types. Therefore, the figures over soil are not shown in the main text, but are provided in the Supplementary Materials.

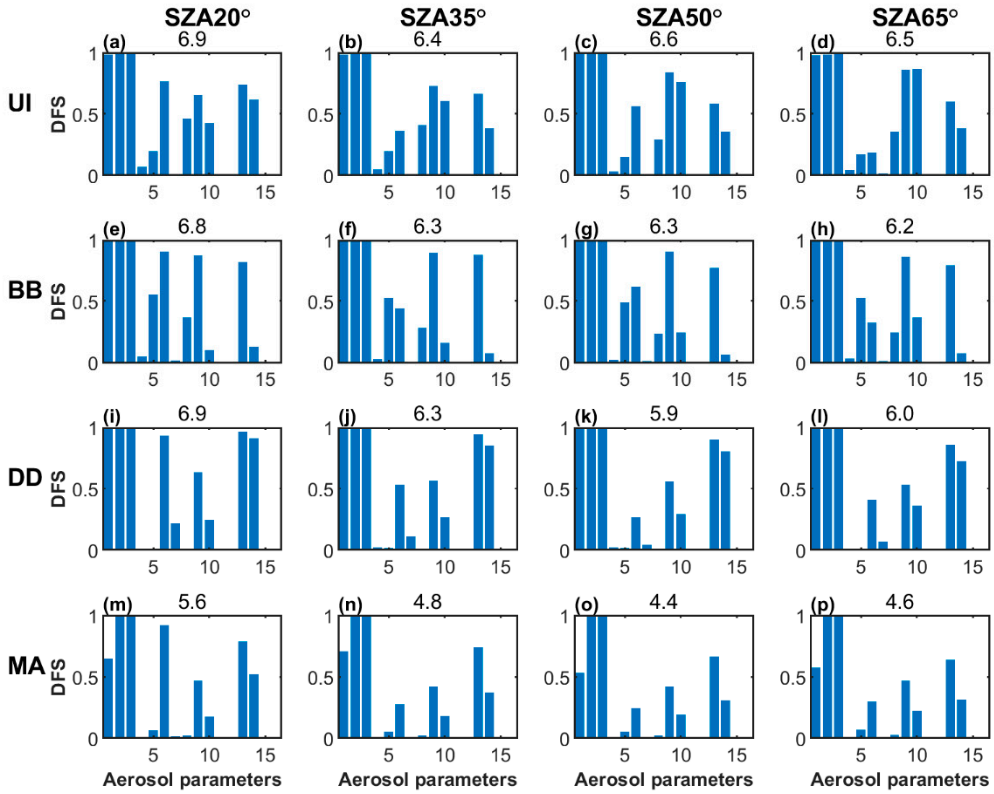

Figure 6. (**a**–**p**) Degrees of freedom for signal (DFS) of each aerosol parameter in the CO_2 retrieval, if all aerosol parameters are retrieved simultaneously over vegetation. The x-axis represents 16 aerosol parameters, as shown from bottom to top in Figure 5a. The four rows are the four aerosol types and different columns illustrate the DFSs at different SZAs. The number over each subfigure is the total DFS of all aerosol parameters.

Overall, four to seven pieces of independent aerosol information could be retrieved from the TanSat observations for the different aerosol types. In other words, the simultaneous retrieval of four to seven aerosol parameters during CO_2 retrieval is more reasonable than retrieving all 16 aerosol parameters. If the aerosol parameters in the CO_2 retrieval state vector are combined in different ways, the induced interference errors may also change; additionally, the forward model parameter errors from the nonretrieved aerosol parameters should be considered. Therefore, even though the number of retrievable aerosol parameters is determined, the requirement to select and retrieve four to seven aerosol parameters simultaneously is also a significant problem. The impact of changing the aerosol models used in the XCO_2 retrieval is analyzed in the next section.

5. The Impact of Different Aerosol Models

As stated in the previous section, the retrieval of different parameters for the aerosol model will affect XCO_2 retrieval, which can be quantified as the CO_2 information and the aerosol-induced retrieval errors in the XCO_2. In this section, the CO_2 information is first estimated for the synchronous retrieval of different aerosol models with different parameters. Furthermore, all components of the XCO_2 retrieval error, including the smoothing, measurement, interference, and forward model parameter errors (as in Section 2.2), are discussed when the aerosol parameters included in the state vector change. To underline the errors caused by aerosols, the interference errors and forward model parameter errors associated with the aerosol parameters are compared among the different retrieval scenarios. Finally, the guiding principle for optimizing the aerosol model for correction of the aerosol effects on XCO_2 retrieval is determined.

5.1. DFS of CO_2

Based on the theory and equations set out in Section 2, the averaging kernel matrix **A** of CO_2 retrieval is calculated. The diagonal elements of **A** correspond to the DFS of each parameter in the state vector; then, those elements related to the CO_2 profile are summarized as CO_2 DFS. The dependence of CO_2 DFS on the number of aerosol parameters to be retrieved is shown in Figure 7 for the different aerosol types. When the number of aerosol parameters to be retrieved is fixed, various combination groups of parameters are available. Each whisker-box in Figure 7 represents the statistical distribution of DFS for all groups, with a constant number of retrieved aerosol parameters.

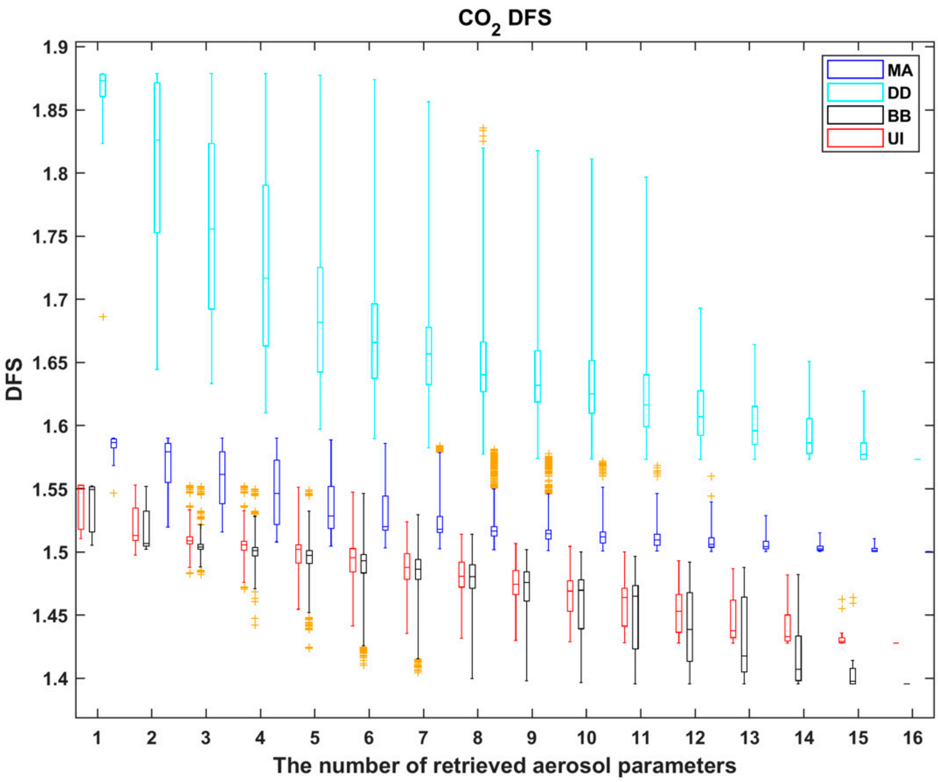

Figure 7. XCO_2 DFS for four types of aerosols when the number of retrieved aerosol parameters ranges from 1 to 16. The SZA is 20° and the surface type is vegetation. For each box, the central mark indicates the median, and the bottom and top edges of the box indicate the 25th (q1) and 75th (q3) percentiles, respectively. The whiskers extend from q3+4×(q3−q1) to q1−4×(q3−q1), and the remaining data extending this range are plotted as outliers using the '+' symbol.

Figure 7 shows that the DFS of CO_2 ranges from 1.4 to 1.9 when different aerosol parameters are retrieved, suggesting that fewer than two CO_2 profiles could be retrieved. A comparison of the four aerosol types reveals that the CO_2 DFS for DD was the largest, at 1.6–1.9 DFS, while slightly less CO_2 DFS for UI and BB shows the scramble for more aerosol DFS due to the larger AOD. As the number of aerosol parameters involved in the CO_2 retrieval changes from 1 to 16, the mean CO_2 DFS decreases, especially in the case of DD with a reduction of approximately 0.3 DFS. In contrast, the CO_2 DFS for MA is only slightly reduced, by approximately 0.1. Because the range of the CO_2 DFS expands when there are more aerosol parameter combination groups with the same number of parameters, careful consideration must be given to the selection of parameters. In conclusion, if more aerosol parameters are added during the retrieval, the CO_2 information will decrease to the detriment of the XCO_2 retrieval. Therefore, in combination with the aerosol information analysis presented in Section 4.2, it is more appropriate for the CO_2 retrieval to be limited to four to seven simultaneous aerosol parameters. The question of which aerosol parameters are most appropriate for retrieval will be discussed in the following section.

5.2. Components of XCO_2 Retrieval Errors

To assess the impact of different aerosol combination groups while maintaining a constant number of parameters, all components of the XCO_2 retrieval error are compared in Figure 8; the number of aerosol parameters to be retrieved varied from four to seven, which was in accordance with the findings above. Each subfigure illustrates the distribution of the errors for all retrieved aerosol parameter combination groups. Both the forward model parameter error and the interference error are assumed to be aerosol-related only.

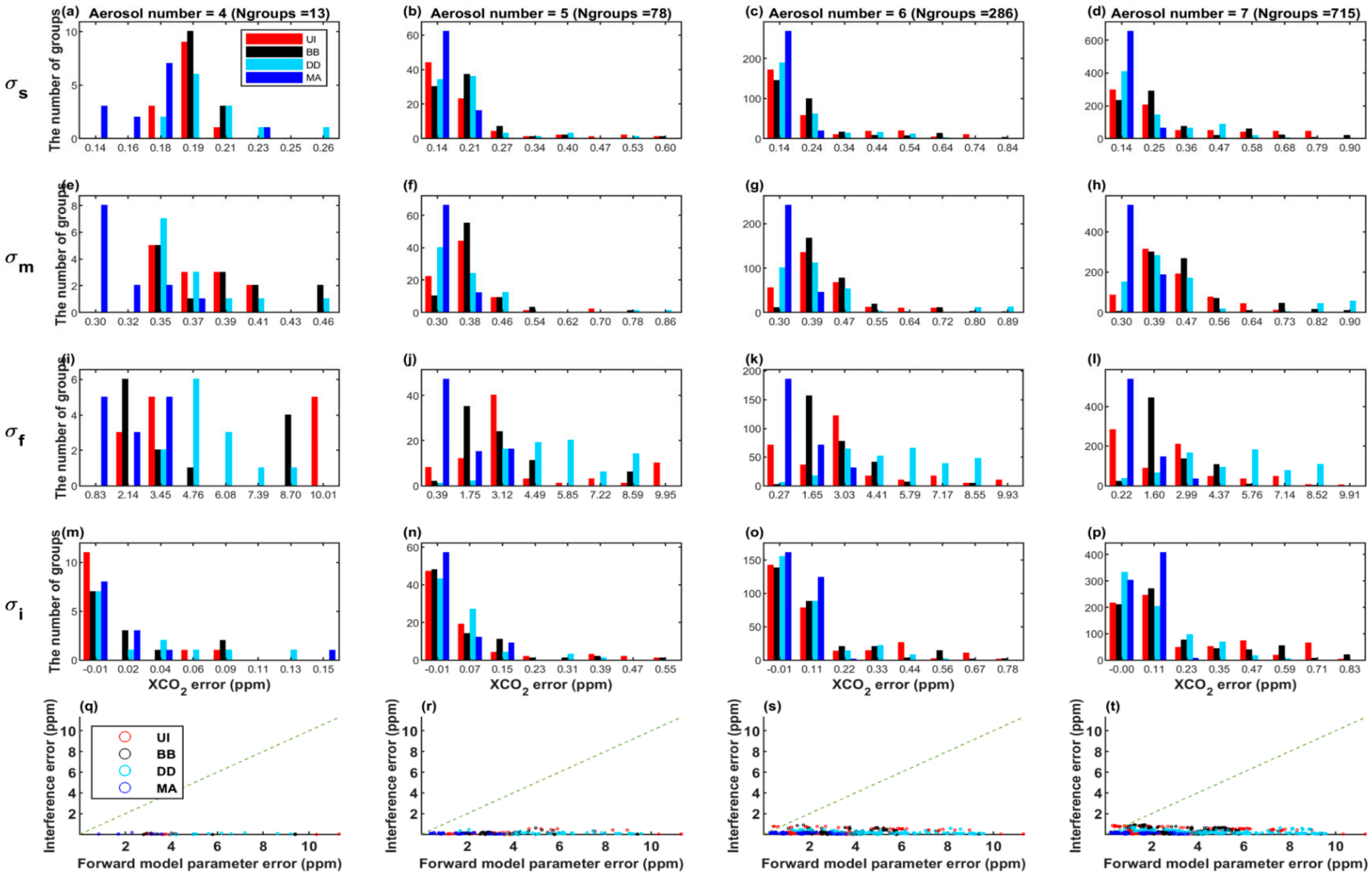

Figure 8. The histograms of the smoothing errors (**a**–**d**), measurement errors (**e**–**h**), forward model parameter errors (**i**–**l**) and interference errors (**m**–**p**) for four to seven retrieved aerosol parameters (columns from left to right), as well as the comparison of the interference error and forward model parameter error in corresponding cases (**q**–**t**). When a different number of retrieved aerosol parameters is selected, the three parameters of AOD, the peak height and width of aerosol profile (H_p and H_w) are always included. Different colorful bars and circles represent the four aerosol types. The dashed lines in (**q**–**t**) illustrate the interference errors equal to the forward model parameter errors.

Generally, the smoothing, measurement, and interference errors fall within a similar range that is smaller than the forward model parameter error. Although the total number of possible aerosol combination groups (shown in Figure 8) increases as the number of retrieved aerosol parameters changes from four to seven, there is a greater fraction of groups with larger smoothing, measurement and interference errors. In contrast, the number of groups increases similarly in all error bins in terms of the forward model parameter error, due to the larger error range.

When the number of retrieved aerosol parameters is held constant among the different aerosol parameter combination groups, most show smaller errors, particularly in the case of MA. In contrast, in the DD case, more group errors are close to the median, especially for the forward model parameter error (Figure 8i–l). On average, all error types are smaller for MA than for other aerosol types, owing to the low AOD. For UI and BB aerosols, the errors are slightly larger, while in the DD case, more groups have larger forward model parameter errors. That is, the distribution of the CO_2 forward model parameter error for DD is more uniform. The distinction of the forward model parameter errors between different aerosol parameter combination groups is more pronounced than other error components (Figure 8i–l). Additionally, the interference errors exhibit significantly more differences in response to changes in the retrieved aerosol parameters than other errors, especially when more parameters are retrieved (Figure 8p). Overall, the distribution of the interference error changes the most when the number of retrieved aerosol parameters increases.

We also identified errors related to aerosol parameter uncertainties, i.e., the forward model parameter and interference errors, and compared these errors among the parameter combination groups (Figure 8q–t). The interference error was always lower than 2 ppm, whereas the forward model parameter error ranged from less than 1 ppm to more than 12 ppm. The forward model parameter error always far exceeds the corresponding interference error, except in some cases when six or seven aerosol parameters are retrieved. Therefore, the total retrieval error of XCO_2 induced by aerosols depends primarily on the forward model parameter error. Although more cases show larger interference errors when retrieving more aerosol parameters, there remain more aerosol parameter combination groups with small forward model parameter errors. Thus, the retrieval of seven aerosol parameters is better for reducing the total XCO_2 retrieval error associated with aerosols (five for MA). Additionally, the forward model error exhibits a larger range for DD and UI than other aerosol types, indicating a greater impact on CO_2 retrieval.

In conclusion, the effect of DD on CO_2 retrieval exceeds that of other aerosol types. The stronger scattering of DD results in larger interference for CO_2 retrieval error. To reduce the aerosol effect on CO_2 retrieval, we sought to identify an aerosol model that would permit a large amount of CO_2 information while simultaneously minimizing the total XCO_2 errors generated from the aerosol parameters, which include both the forward model error and interference error. Considering that fewer aerosol-induced retrieval errors of XCO_2 occur in cases with more retrieved aerosol parameters, the retrieval of seven aerosol parameters is recommended for UI, BB and DD, but only five parameters are recommended for MA due to the lower amounts of aerosol information. When the number of aerosol parameters to be retrieved has been determined, the selection of different aerosol parameter combination groups depends on the comparison of the sum of the forward model parameter errors and the interference errors.

6. Optimization of the Aerosol Model

Considering the large amounts of AOD, H_p, and H_w information in all cases (Section 4.2), these three parameters were retrieved, and the other parameters remained to be determined. To derive the aerosol model with the most appropriate seven parameters for retrieval (five for MA), the forward model parameter and interference errors for the different aerosol parameter combination groups including AOD, H_p, and H_w were compared (Figure 9). Given the small range of CO_2 DFS in these groups (Figure 7), the XCO_2 retrieval error is used as the selection criteria. We sought to select those aerosol parameter groups with the lowest XCO_2 errors; thus, only the XCO_2 aerosol-induced errors under 4 ppm are presented in Figure 9.

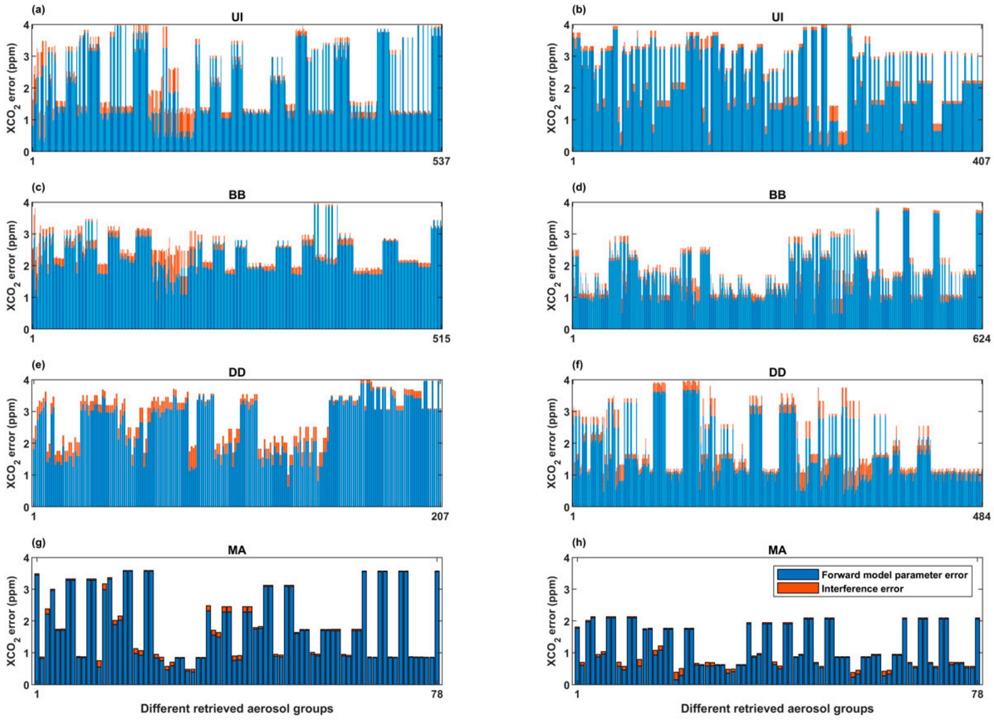

Figure 9. Comparison of interference and forward model parameter errors for different aerosol parameter groups in Figure 8 when the number of retrieved aerosol parameters is maintained at seven for UI, BB and DD aerosol, and five for MA, with the total errors from aerosol parameters being smaller than 4 ppm. The left column is for vegetation (**a**,**c**,**e**,**g**) and the right column is for soil (**b**,**d**,**f**,**h**). The four rows represent the four types of aerosols. The x-axis represents the index of different aerosol parameter groups and the numbers at the end of the x-axis are the total number of groups.

In Figure 9, for vegetation, it can be seen that although the forward model parameter errors of most of the aerosol parameter combination groups exceed the corresponding interference errors (Figure 8q–t), there are still some groups with errors that are close to the interference errors, particularly in the cases of UI and BB aerosols. However, with regard to DD and MA, the total XCO_2 errors are dominated by the forward model parameter error in nearly all groups (Figure 9c,d). The number of aerosol parameter combination groups showing lower total XCO_2 aerosol-induced errors for DD is 207, which is significantly less than for the UI (n = 537) and BB (n = 515) aerosols. The total number of combination groups for MA is only 78, which is less than that for the other three aerosol types, due to only five aerosol parameters being retrieved. In other words, the aerosol-induced XCO_2 errors of all MA groups are smaller than 4 ppm, and most of the errors are under 2 ppm. Additionally, the lowest error of DD combination groups is under 2 ppm, and those for UI and BB aerosols are close to 2 ppm.

Comparing two surface types, the aerosol-induced XCO_2 errors over soil are apparently lower than those over vegetation for the BB, DD and MA aerosols at only half. Additionally, regarding the value of the total error, a greater number of groups with low errors is found over soil than over vegetation. However, for UI aerosol, most groups have similar XCO_2 errors over soil as those over vegetation, which is approximately 1.5 to 3.5 ppm. Furthermore, for the soil surface, the number of groups with errors that are lower than 4 ppm is also less at only 407. Notably, the lowest XCO_2 error over soil is lower than that over vegetation at only approximately 0.5 ppm (Figure 9a,b). This finding means that for the UI aerosol over soil, the choice of the aerosol parameter combination group is more important for reducing the XCO_2 error. For the other three aerosol types, the XCO_2 errors over vegetation still serve as the main criteria for selecting aerosol groups that are suitable for all land surfaces.

As Figure 9 illustrates, we sought to select the aerosol parameter combination group with the lowest number of XCO_2 aerosol-induced errors for all aerosol types and all surface types. All of the aerosol parameter combination groups shown in Figure 9 were sorted from low to high by the total number of XCO_2 aerosol-induced errors for each aerosol type. The first combination group was chosen as the best aerosol model for the CO_2 retrieval algorithm. Table 5 summarizes the first few combination groups and their total aerosol-induced XCO_2 retrieval errors for all aerosol types and both surfaces. For MA, it would evidently be better to retrieve five aerosol parameters, namely, AOD, H_p, H_w, r_{eff}^c, a_r^c, for the CO_2 retrieval algorithms with an aerosol-induced XCO_2 error of less than 0.5 ppm. For the other three types of aerosols, three aerosol parameter combination groups with low errors were selected as Groups 1, 2, and 3 (Table 5). In these groups, six of the seven aerosol parameters were identical: AOD, H_p, H_w, r_{eff}^c, a_r^f and a_r^c; this finding indicates that in addition to the AOD and the aerosol profile, the size parameter of the coarse aerosol and the real part parameter of the refractive index of both modes should also be retrieved. There was a little difference among the groups in the remaining aerosol parameters, which were fmf, size parameter of fine mode, and the other refractive index coefficient. In a comparison of the total aerosol-induced XCO_2 errors, the differences in UI and DD among Groups 1–3 were less than 0.1 ppm and more than 0.1 ppm for BB. Comparing different surface types, the errors over soil for the three groups are apparently smaller than those over vegetation except for UI. As we demonstrated in Figure 9, the XCO_2 error caused by the UI aerosol over soil shows a larger difference to even more than 0.8 ppm among Groups 1–3 when the aerosol group changes. Despite the lower error of Group 2 for UI and DD over soil than Group 1, BB aerosol leads to greater XCO_2 uncertainty for the vegetation surface, whcih exceeds 2 ppm. Considering the generality, we recommend Group 1 as the optimal aerosol modelto maintain the aerosol-induced XCO_2 error below 1.7 ppm for all three aerosol types and both surface types.

If additional information concerning aerosol size or optical properties are obtained prior to retrieval, such as from CAPI measurements or MODIS inversion products, so that DD may be distinguished from UI and BB, Group 4 is recommended. In this group, two different aerosol parameters, including the size and refractive index parameter, are selected for DD and the other two aerosol types, as shown in Table 5. Consequently, the parameters pertaining to fine mode aerosols for UI and BB, such as b_r^f and v_{eff}^f, are replaced by similar parameters but of coarse mode for DD as the optimal model, which is mainly due to the large particle size of the DD aerosol. Accordingly, the total aerosol-induced XCO_2 errors are clearly reduced for DD and UI.

Table 5. The aerosol parameter combination groups for each aerosol type with the lowest total aerosol-induced XCO_2 retrieval and corresponding errors.

	Aerosol Types	Group 1	Group 2	Group 3	Group 4
Retrieved aerosol parameters [1]	UI BB	(AOD, H_p, H_w, v_{eff}^f, r_{eff}^c, a_r^f, a_r^c)	(AOD, H_p, H_w, r_{eff}^c, a_r^f, b_r^f, a_r^c)	(AOD, H_p, H_w, r_{eff}^c, fmf, a_r^f, a_r^c)	(AOD, H_p, H_w, v_{eff}^f, a_r^f, b_r^f, a_r^c)
	DD				(AOD, H_p, H_w, r_{eff}^c, a_r^f, a_r^c, b_r^c)
	MA	(AOD, H_p, H_w, r_{eff}^c, a_r^c)			
Total aerosol-induced XCO_2 retrieval errors (ppm)	UI	1.1986/1.3702 [2]	1.2907/0.5883	1.2463/1.4326	1.1998/0.7986
	BB	1.5241/0.7762	2.0871/0.9462	1.9109/0.9569	1.6671/1.0424
	DD	1.6421/1.1227	1.5595/1.0250	1.6371/1.1246	1.0138/0.9929
	MA	0.4821/0.4836			

[1] The aerosol parameter abbreviations are consistent with those in Figure 5a. [2] The values front of the symbol "/" represent results for vegetation surface and those behind are for soil surface.

Finally, AOD and two aerosol profile parameters (H_p and H_w), as well as one particle size parameter (r_{eff}^c) and one real part coefficient of refractive index (a_r^c) for coarse particles are recommended for the CO_2 retrieval state vector for all aerosol types to minimize aerosol-induced errors. Owing to a larger amount of aerosol information for the other three aerosol types except MA, two more parameters of fine particles including size and real refractive index parameters (v_{eff}^f and a_r^f) could also be retrieved. If additional aerosol information can be obtained from other satellites or instruments to distinguish coarse dust aerosols, the optimal aerosol parameter combination for DD contains the size parameter and real refractive index coefficient for coarse mode (r_{eff}^{c} and b_r^{c}) rather than fine particles (v_{eff}^{f} and b_r^{f}) for the other three types. Under these circumstances, a further decrease is observed in the aerosol-induced XCO_2 retrieval errors for DD.

7. Discussions

In this paper, we only consider the mean aerosol loading with constant AOD for each aerosol type, according to the statistical analysis of AERONET inversion products. Would the change in AOD describing different air pollution levels for one aerosol type influence the optimal aerosol model selection for CO_2 retrieval? To address this issue, the information and a posteriori error are compared when AOD ranges from 0.1 to 2.0 at 440 nm (Figure 10). The aerosol DFS becomes larger as the AOD increases, whereas there is a threshold of aerosol DFS. As soon as the aerosol DFS reaches the threshold, increasing the AOD could add little DFS (8.0 DFS in Figure 10f). Generally, the change in the aerosol DFS caused by AOD variation is not more than 1.0 (Figure 10f). Furthermore, comparing the DFSs of different aerosol parameters (Figure 10a–e), each parameter has a larger DFS when the AOD increases, whereas those parameters with larger DFSs change little with AOD. Therefore, although, adding one more retrieved aerosol parameter is more appropriate in those cases with 1.0 more DFS, the optimal aerosol model in this study has already accounted for the most greatest amount of XCO_2 retrieval errors from aerosols. If the AOD is small and shows thin aerosol pollution, the interference of aerosol uncertainties for CO_2 retrieval does not require much focus. Considering the generality of the aerosol model, the variation in AOD would not interfere with the selection of the retrieved aerosol parameters group.

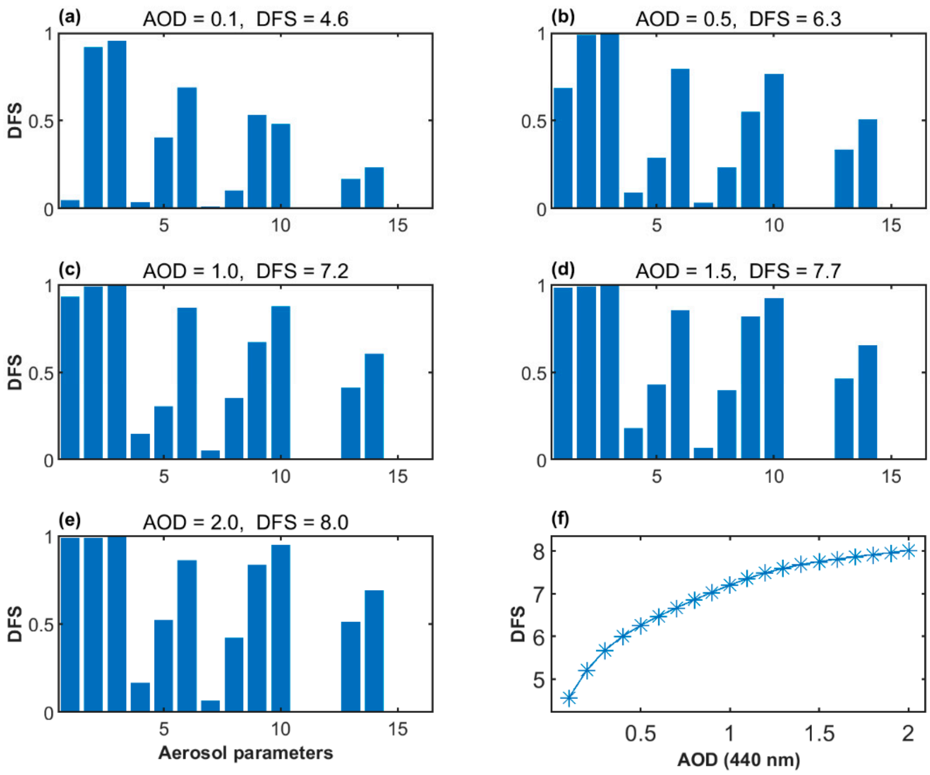

Figure 10. The DFS of each aerosol parameter (**a**–**e**) for different AODs over vegetation similar to Figure 6. (**f**) shows the variation in the total aerosol DFS with the change in AOD from 0.1 to 2.0 at 440 nm.

Similarly, the aerosol vertical profile mainly affects the total aerosol DFS and the profile parameter information. Given that the height of the aerosol layer changes the absorption of O_2, the measurements in the TanSat O_2-A band always contain a large amount of information about aerosol profile parameters, no matter where the aerosol is concentrated. Different aerosol profiles have less impact on microphysical parameters information than different aerosol types and their interference errors in XCO_2, meaning that not much attention to the aerosol profile is required when choosing the optimal aerosol model. Considering the limited aerosol information contained in the spectra, an aerosol model with a fixed vertical distribution shape is used instead of retrieving aerosol loading at each layer, and thus, more information would be distributed to the microphysical parameters. In addition, this research focuses on TanSat nadir observations over land, which is assumed to be a combination of both soil and vegetation surfaces. There are still a few areas of land covered by snow or ice with higher reflectances, especially at high latitudes. Based on comparisons of vegetation and soil surfaces, uncertainties in XCO_2 caused by aerosols decrease as surface reflectance increases. Thus, over snow or ice, the interference from aerosols in CO_2 retrieval is so small that this interference would not affect our decision to use the optimal aerosol model. For some water surfaces on land with lower surface reflectance, the radiation reflected by the surface is so small that it is not used to retrieve CO_2. Furthermore, only observations under clear sky are considered in this study, which is a simple assumption for real atmosphere. Based on the cloud contamination model involving cirrus, which has been implemented in the TanSat CO_2 retrieval algorithm, we do not consider complex situations involving thin clouds here.

With the methodology used in our study, we analyzed the information content in measured spectra and estimated the retrieval errors directly from the spectrum residual and the status of the measurements and atmosphere, without a practical retrieval process. Compared with previous studies [24,55], the aerosol DFS in our study is larger depending on our the a priori and measurement error assumption, as well as the fixed aerosol model. The sensitivities of the spectrum to the microphysical aerosol parameters included in this study show distinct patterns with CO_2, also causing larger information of aerosol parameters. The strong constrain and low uncertainty of surface model is another reason for large aerosol DFS. Even though, we believe our research still caught the relationship between aerosol model and CO_2 retrieval. One the other hand, although this optimal estimation method has a limitation of an approximately linear assumption within the region bounded by its uncertainty, this method has been used in many studies related to trace gases and aerosol retrieval and has achieved a good performance in algorithm design and error analysis, and these previous studies include those of Hasekamp and Landgraf [34], Connor et al. [17], Martynenko et al. [36], Frankenberg et al. [37], and Connor et al. [16]. Similar to Connor et al. [16], an additional kind of error, namely, the forward model parameter error, is added in our analysis to depict the distinction between the simulation and retrieval setup.

8. Conclusions

In this study, we have focused on optimizing the aerosol model for the CO_2 retrieval algorithm based on TanSat observations, which was in accordance with information estimation and error analysis. The hyperspectra of TanSat's three NIR bands, and the corresponding weighting functions with respect to the retrieved parameters, were simulated by a forward radiative transfer model, VLIDORT. Our simulations considered four types of aerosols, comprising fine and coarse particles with different microphysical properties over two types of land with different surface reflectance, vegetation and soil. These aerosol microphysical properties were obtained from the most recent five-year AERONET inversion products for several sites, similar to our previous study. The surface reflection was characterized by the Ross–Li BRDF model using MODIS products. The information content of the parameters retrieved from observations was represented by the DFS. The a posteriori error in XCO_2 was composed of four components, including the smoothing error, measurement error, forward model parameter error, and interference error, which could be calculated from the *a priori* assumptions by applying the optimal estimation theory. To reduce the effects of aerosols on CO_2 retrieval, the aerosol-related components of the XCO_2 retrieval error were given focus.

If all 16 aerosol parameters are retrieved synchronously with CO_2 information, two size distribution parameters for fine and coarse particles (r_{eff}, v_{eff}), real refractive index coefficient of fine mode (a_r^f)

and fmf cause the largest interference errors in the XCO_2, reaching 0.2–0.8 ppm. The total interference errors of all aerosol parameters range from 0.2 to 1.0 ppm and increase with smaller SZAs due to the shorter light path. MA parameters cause the fewest interference errors with no more than 0.3 ppm. The lower surface reflectance for vegetation indicates the larger impact of aerosols on XCO_2 retrieval. However, not all aerosol parameters could be retrieved from the TanSat hyperspectral observations, as there were only 4–7 DFSs serving as aerosol parameters over both surface types. When more aerosol parameters in the algorithm were simultaneously retrieved, the CO_2 information decreased with the lower DFS. The principle of optimization is to minimize the aerosol-induced XCO_2 error components while retaining a large amount of CO_2 information. Combined with the estimated aerosol information, retrieval of four to seven aerosol parameters is more reasonable.

Of the four XCO_2 retrieval error components, the forward model parameter and interference errors are associated with uncertain aerosol parameters. Overall, aerosol-induced XCO_2 errors are dominated by the forward model parameter error rather than the interference error, due to the larger values of the former. When the number of retrieved aerosol parameters increases from four to seven, more aerosol parameter combination groups have fewer forward model parameter errors, despite hte CO_2 DFS decreasing slightly. Considering a greater reduction in the aerosol-induced XCO_2 error, seven aerosol parameters are deemed the most appropriate for XCO_2 retrieval. For MA, the number of retrieved aerosol parameters should be five because of the low amounts of aerosol information. The XCO_2 errors of different aerosol parameter combination groups vary, even when the number of retrieved aerosol parameters is constant. To minimize aerosol impact, the total aerosol-induced XCO_2 retrieval errors of different groups with seven retrieved aerosol parameters (five for MA) were compared and sorted from low to high. Ultimately, the aerosol parameter combination group with the lowest aerosol-induced XCO_2 errors was selected. Considering the feasibility and generality of the aerosol model for all aerosol types and land surface types, the aerosol parameters of AOD, H_p, H_w, v_{eff}^f, r_{eff}^c, a_r^f and a_r^c are recommended to be retrieved simultaneously with CO_2, except in the case of MA, which only requires the retrieval of five parameters (AOD, H_p, H_w, r_{eff}^c and a_r^c). If additional information on aerosol properties could be added from other sources to initially distinguish DD from other aerosol types, two microphysical parameters of coarse mode aerosol (r_{eff}^c and b_r^c) could be retrieved with fewer XCO_2 errors for DD, which would be in place of the fine particle parameters (v_{eff}^f and b_r^f) for UI and BB.

Overall, the retrieved aerosol parameters in the optimal aerosol model for CO_2 retrieval are determined with fewer aerosol-induced XCO_2 errors and still yield large amounts of CO_2 information. In the next step, the performance of this optimal aerosol model will be verified by running the actual CO_2 retrieval based on the IAPCAS algorithm structure from GOSAT, OCO-2 or TanSat observations. The methods and rules applied to optimize the aerosol model in this study may also be applicable to CO_2 retrieval from other satellites. This research forms a basis for enhancing the accuracy of high-precision CO_2 retrieval algorithms. The optimal aerosol model proposed here may be applied to future CO_2 retrievals based on realistic TanSat data.

Supplementary Materials: The following are available online at http://www.mdpi.com/2072-4292/11/9/1061/s1, Figure S1: The Jacobians with respect to all BRDF kernel coefficients, Figure S2: The comparison of the interference error from each aerosol parameter between over vegetation and soil. Figure S3. The comparison of DFS of each aerosol parameter for four aerosol types over vegetation and soil. Figure S4. The SNR curves examined in the laboratory for each band of TanSat ACGS. Figure S5. The surface reflectivity estimated by Ross-Li BRDF model at different observation geometries.

Author Contributions: Conceptualization, X.C. and D.Y.; Methodology, Y.L. and D.Y.; Software, Z.C. and D.Y.; Validation, X.C. and D.Y.; Formal Analysis, X.C.; Investigation, X.C. and D.Y.; Resources, M.W.; Data Curation, X.C.; Writing-Original Draft Preparation, X.C.; Writing-Review & Editing, D.Y.; Visualization, X.C.; Supervision, H.C.; Project Administration, M.W.; Funding Acquisition, Y.L.

Funding: This research was funded by the National Key R&D Program of China (No. 2017YFB0504001), the Key Research Program of the Chinese Academy of Sciences (ZDRW-ZS-2019-1), the China Postdoctoral Science Foundation, the National Key R&D Program of China (No. 2016YFA0600203), and the External Cooperation Program of the Chinese Academy of Sciences (Grant No. GJHZ1507).

Acknowledgments: The authors would like to thank PI and CI of AERONET four sites: Zhengqiang Li of Beijing_RADI site, Brent Holben and Brent Holben of Alta_Floresta site, Didier Tanri of Capo_Verde site and Brent Holben, Chuck McClain and Robert Frouin of Lanai site, for providing measurement data. They also thank TanSat mission and team for supporting this work.

Conflicts of Interest: The authors declare no conflict of interest. The funders had no role in the design of the study; in the collection, analyses, or interpretation of data; in the writing of the manuscript, or in the decision to publish the results.

References

1. Team, C.W.; Pachauri, R.K.; Meyer, L.A. *Climate Change 2014: Synthesis Report*; IPCC Press Office: Geneva, Switzerland, 2014; p. 151.
2. Stocker, T.F.; Qin, D.; Plattner, G.K.; Tignor, M.; Allen, S.K.; Boschung, J.; Nauels, A.; Xia, Y.; Bex, V.; Midgley, P.M. *Climate Change 2013: The Physical Science Basis. Contribution of Working Group I to the Fifth Assessment Report of the Intergovernmental Panel on Climate Change*; Cambridge University Press: Cambridge, UK, 2013.
3. Kuze, A.; Suto, H.; Nakajima, M.; Hamazaki, T. Thermal and near infrared sensor for carbon observation Fourier-transform spectrometer on the Greenhouse Gases Observing Satellite for greenhouse gases monitoring. *Appl. Opt.* **2009**, *48*, 6716. [CrossRef] [PubMed]
4. Yokota, T.; Yoshida, Y.; Eguchi, N.; Ota, Y.; Tanaka, T.; Watanabe, H.; Maksyutov, S. Global Concentrations of CO_2 and CH_4 Retrieved from GOSAT: First Preliminary Results. *SOLA* **2009**, *5*, 160–163. [CrossRef]
5. Nobuta, K.; Morino, I.; Yoshida, Y.; Ota, Y.; Eguchi, N.; Kikuchi, N.; Tran, H.; Yokota, T. Retrieval algorithm for CO_2 and CH_4 column abundances from short-wavelength infrared spectral observations by the Greenhouse gases observing satellite. *Atmos. Meas. Tech.* **2011**, *4*, 717–734.
6. Maksyutov, S.; Takagi, H.; Valsala, V.K.; Saito, M.; Oda, T.; Saeki, T.; Belikov, D.A.; Saito, R.; Ito, A.; Yoshida, Y.; et al. Regional CO_2 flux estimates for 2009–2010 based on GOSAT and ground-based CO_2 observations. *Atmos. Chem. Phys. Discuss.* **2013**, *13*, 9351–9373. [CrossRef]
7. Deng, F.; Jones, D.B.A.; O'Dell, C.W.; Nassar, R.; Parazoo, N.C. Combining gosat xco2 observations over land and ocean to improve regional CO_2 flux estimates. *J. Geophys. Res. Atmos.* **2016**, *121*, 1896–1913. [CrossRef]
8. Eldering, A.; O'dell, C.W.; Wennberg, P.O.; Crisp, D.; Gunson, M.R.; Viatte, C.; Avis, C.; Braverman, A.; Castano, R.; Chang, A.; et al. The Orbiting Carbon Observatory-2: first 18 months of science data products. *Atmos. Meas. Tech.* **2017**, *10*, 549–563. [CrossRef]
9. Eldering, A.; Wennberg, P.O.; Crisp, D.; Schimel, D.S.; Gunson, M.R.; Chatterjee, A.; Liu, J.; Schwandner, F.M.; Sun, Y.; O'Dell, C.W.; et al. The Orbiting Carbon Observatory-2 early science investigations of regional carbon dioxide fluxes. *Science* **2017**, *358*, eaam5745. [CrossRef]
10. Liu, Y.; Yang, D.; Cai, Z. A retrieval algorithm for TanSat XCO_2 observation: Retrieval experiments using GOSAT data. *Chin. Sci.* **2013**, *58*, 1520–1523. [CrossRef]
11. Li, Z.; Lin, C.; Li, C.; Wang, L.; Ji, Z.; Xue, H.; Wei, Y.; Gong, C.; Gao, M.; Liu, L. Prelaunch spectral calibration of a carbon dioxide spectrometer. *Meas. Sci. Technol.* **2017**, *28*, 6. [CrossRef]
12. Zhang, H.; Zheng, Y.; Lin, C.; Wang, W.; Wang, Q.; Li, S. Laboratory spectral calibration of TanSat and the influence of multiplex merging of pixels. *Int. J. Sens.* **2017**, *38*, 3800–3816. [CrossRef]
13. Yang, D.; Liu, Y.; Cai, Z.; Chen, X.; Yao, L.; Lu, D. First Global Carbon Dioxide Maps Produced from TanSat Measurements. *Adv. Atmos. Sci.* **2018**, *35*, 621–623. [CrossRef]
14. Rayner, P.J.; O'Brien, D.M. The utility of remotely sensed CO_2 concentration data in surface source inversions. *Geophys. Lett.* **2001**, *28*, 175–178. [CrossRef]
15. Aben, I.; Hasekamp, O.; Hartmann, W. Uncertainties in the space-based measurements of CO_2 columns due to scattering in the Earth's atmosphere. *J. Quant. Spectrosc. Radiat. Transf.* **2007**, *104*, 450–459. [CrossRef]
16. Connor, B.; Boesch, H.; McDuffie, J.; Taylor, T.; Fu, D.; Frankenberg, C.; O'dell, C.; Payne, V.; Gunson, M.; Pollock, R.; et al. Quantification of Uncertainties in OCO-2 Measurements of XCO_2: Simulations and Linear Error Analysis. *Atmos. Meas. Tech. Discuss.* **2016**, *9*, 1–30. [CrossRef]
17. Connor, B.J.; Boesch, H.; Toon, G.; Sen, B.; Miller, C.; Crisp, D. Orbiting Carbon Observatory: Inverse method and prospective error analysis. *J. Geophys. Res. Biogeosci.* **2008**, *113*. [CrossRef]
18. O'dell, C.W.; Connor, B.; Bosch, H.; O'brien, D.; Frankenberg, C.; Castano, R.; Christi, M.; Eldering, D.; Fisher, B.; Gunson, M.; et al. The ACOS CO_2 retrieval algorithm – Part 1: Description and validation against synthetic observations. *Atmos. Meas. Tech.* **2012**, *5*, 99–121. [CrossRef]

19. O'dell, C.W.; Eldering, A.; Wennberg, P.O.; Crisp, D.; Gunson, M.R.; Fisher, B.; Frankenberg, C.; Kiel, M.; Lindqvist, H.; Mandrake, L.; et al. Improved retrievals of carbon dioxide from Orbiting Carbon Observatory-2 with the version 8 ACOS algorithm. *Atmos. Meas. Tech.* **2018**, *11*, 6539–6576. [CrossRef]
20. Chen, X.; Wang, J.; Liu, Y.; Xu, X.; Cai, Z.; Yang, D.; Yan, C.-X.; Feng, L. Angular dependence of aerosol information content in capi/tansat observation over land: Effect of polarization and synergy with a-train satellites. *Remote Sens. Environ.* **2017**, *196*, 163–177. [CrossRef]
21. Chen, X.; Yang, D.; Cai, Z.; Liu, Y.; Spurr, R.J.D. Aerosol Retrieval Sensitivity and Error Analysis for the Cloud and Aerosol Polarimetric Imager on Board TanSat: The Effect of Multi-Angle Measurement. *Remote. Sens.* **2017**, *9*, 183. [CrossRef]
22. Yoshida, Y.; Kikuchi, N.; Morino, I.; Uchino, O.; Oshchepkov, S.; Bril, A.; Saeki, T.; Schutgens, N.; Toon, G.C.; Wunch, D.; et al. Improvement of the retrieval algorithm for GOSAT SWIR XCO_2 and XCH_4 and their validation using TCCON data. *Atmos. Meas. Tech.* **2013**, *6*, 1533–1547. [CrossRef]
23. Boesch, H.; Baker, D.; Connor, B.; Crisp, D.; Miller, C. Global Characterization of CO_2 Column Retrievals from Shortwave-Infrared Satellite Observations of the Orbiting Carbon Observatory-2 Mission. *Remote. Sens.* **2011**, *3*, 270–304. [CrossRef]
24. Butz, A.; Hasekamp, O.P.; Frankenberg, C.; Aben, I. Retrievals of atmospheric CO_2 from simulated space-borne measurements of backscattered near-infrared sunlight: accounting for aerosol effects. *Appl. Opt.* **2009**, *48*, 3322. [CrossRef]
25. Butz, A.; Guerlet, S.; Hasekamp, O.; Schepers, D.; Galli, A.; Aben, I.; Frankenberg, C.; Hartmann, J.-M.; Tran, H.; Kuze, A.; et al. Toward accurate CO_2 and CH_4 observations from GOSAT. *Geophys. Lett.* **2011**, *38*, 38. [CrossRef]
26. Torres, O.; Bhartia, P.K.; Herman, J.R.; Gleason, J.; Ahmad, Z. Derivation of aerosol properties from satellite measurements of backscattered ultraviolet radiation: Theoretical basis. *J. Geophys. Res. Biogeosci.* **1998**, *103*, 17099–17110. [CrossRef]
27. Dubovik, O.; Sinyuk, A.; Lapyonok, T.; Holben, B.N.; Mishchenko, M.; Yang, P.; Eck, T.F.; Volten, H.; Muñoz, O.; Veihelmann, B.; et al. Application of spheroid models to account for aerosol particle nonsphericity in remote sensing of desert dust. *J. Geophys. Res. Biogeosci.* **2006**, *111*, 111. [CrossRef]
28. McGarragh, G.R. Combined Multispectral/hyperspectral Remote Sensing of Tropospheric Aerosols for Quantification of Their Direct Radiative Effect. Ph.D. Thesis, Colorado State University, Fort Collins, CO, USA, 2013.
29. Xu, X.; Wang, J.; Yi, W.; Jing, Z.; Torres, O.; Yang, Y.; Marshak, A.; Reid, J.; Miller, S. Passive remote sensing of altitude and optical depth of dust plumes using the oxygen A and B bands: First results from EPIC/DSCOVR at Lagrange-1 point. *Geophys. Res. Lett.* **2017**, *44*, 7544–7554. [CrossRef]
30. Yang, D.; Liu, Y.; Cai, Z.; Deng, J.; Wang, J.; Chen, X. An advanced carbon dioxide retrieval algorithm for satellite measurements and its application to GOSAT observations. *Sci. Bull.* **2015**, *60*, 2063–2066. [CrossRef]
31. Yang, D.; Zhang, H.; Liu, Y.; Chen, B.; Cai, Z.; Lü, D. Monitoring carbon dioxide from space: Retrieval algorithm and flux inversion based on GOSAT data and using CarbonTracker-China. *Adv. Atmos. Sci.* **2017**, *34*, 965–976. [CrossRef]
32. Rodgers, C.D. *Inverse Methods for Atmospheric Sounding-Theory and Practice*; World Scientific Pub Co Pte Lt: Singapore, 2000.
33. Xu, X.; Wang, J. Retrieval of aerosol microphysical properties from AERONET photopolarimetric measurements: 1. Information content analysis. *J. Geophys. Res. Atmos.* **2015**, *120*, 7059–7078. [CrossRef]
34. Hasekamp, O.P.; Landgraf, J. Retrieval of aerosol properties over the ocean from multispectral single-viewing-angle measurements of intensity and polarization: Retrieval approach, information content, and sensitivity study. *J. Geophys. Res. Biogeosci.* **2005**, *110*, 1–16. [CrossRef]
35. Holzer-Popp, T.; Schroedter-Homscheidt, M.; Breitkreuz, H.; Martynenko, D.; Klüser, L. Improvements of synergetic aerosol retrieval for envisat. *Atmos. Chem. Phys.* **2008**, *8*, 7651–7672. [CrossRef]
36. Martynenko, D.; Holzer-Popp, T.; Elbern, H.; Schroedter-Homscheidt, M. Understanding the aerosol information content in multi-spectral reflectance measurements using a synergetic retrieval algorithm. *Atmos. Meas. Tech. Discuss.* **2010**, *3*, 2579–2602. [CrossRef]
37. Frankenberg, C.; Hasekamp, O.; O'dell, C.; Sanghavi, S.; Butz, A.; Worden, J.; O'Dell, C. Aerosol information content analysis of multi-angle high spectral resolution measurements and its benefit for high accuracy greenhouse gas retrievals. *Atmos. Meas. Tech.* **2012**, *5*, 1809–1821. [CrossRef]

38. Geddes, A.; Bosch, H. Tropospheric aerosol profile information from high-resolution oxygen A-band measurements from space. *Atmos. Meas. Tech.* **2015**, *8*, 859–874. [CrossRef]
39. Wang, J.; Xu, X.; Ding, S.; Zeng, J.; Spurr, R.; Liu, X.; Chance, K.; Mishchenko, M. A numerical testbed for remote sensing of aerosols, and its demonstration for evaluating retrieval synergy from a geostationary satellite constellation of GEO-CAPE and GOES-R. *J. Quant. Spectrosc. Radiat. Transf.* **2014**, *146*, 510–528. [CrossRef]
40. Spurr, R. LIDORT and VLIDORT: Linearized pseudo-spherical scalar and vector discrete ordinate radiative transfer models for use in remote sensing retrieval problems. *Light Scatt. Rev. 3* **2008**, 229–275.
41. Liu, Y.; Wang, J.; Yao, L.; Chen, X.; Cai, Z.; Yang, D.; Yin, Z.; Gu, S.; Tian, L.; Lu, N.; et al. The TanSat mission: Preliminary global observations. *Sci. Bull.* **2018**, *63*, 1200–1207. [CrossRef]
42. Peters, W.; Jacobson, A.R.; Sweeney, C.; Andrews, A.E.; Conway, T.J.; Kenneth, M.; Miller, J.B.; Bruhwiler, L.M.P.; Gabrielle, P.; Hirsch, A.I. An atmospheric perspective on north american carbon dioxide exchange: Carbontracker. *Proc. Natl. Acad. Sci. USA* **2007**, *104*, 18925–18930. [CrossRef]
43. Schaaf, C.B.; Gao, F.; Strahler, A.H.; Lucht, W.; Li, X.; Tsang, T.; Strugnell, N.C.; Zhang, X.; Jin, Y.; Muller, J.-P.; et al. First operational BRDF, albedo nadir reflectance products from MODIS. *Remote Sens. Environ.* **2002**, *83*, 135–148. [CrossRef]
44. Schaaf, C.; Strahler, A.; Lucht, W. An algorithm for the retrieval of albedo from space using semiempirical BRDF models. *IEEE Trans. Geosci. Sens.* **2000**, *38*, 977–998.
45. Von Hoyningen-Huene, W.; Freitag, M.; Burrows, J.B. Retrieval of aerosol optical thickness over land surfaces from top-of-atmosphere radiance. *J. Geophys. Res. Biogeosci.* **2003**, *108*, 4260. [CrossRef]
46. Wanner, W.; Strahler, A.H.; Li, X. On the derivation of kernels for kernel-driven models of bidirectional reflectance. *J. Geophys. Res. Biogeosci.* **1995**, *100*, 21077. [CrossRef]
47. Wanner, W.; Strahler, A.H.; Lewis, P.; Muller, J.-P.; Schaaf, C.L.B.; Barnsley, M.J.; Hu, B.; Muller, J.; Li, X. Global retrieval of bidirectional reflectance and albedo over land from EOS MODIS and MISR data: Theory and algorithm. *J. Geophys. Res. Biogeosci.* **1997**, *102*, 17143–17161. [CrossRef]
48. Waquet, F.; Cairns, B.; Knobelspiesse, K.; Chowdhary, J.; Travis, L.D.; Schmid, B.; Mishchenko, M.I. Polarimetric remote sensing of aerosols over land. *J. Geophys. Res. Biogeosci.* **2009**, *114*, 114. [CrossRef]
49. Mishchenko, M.I.; Cairns, B.; Kopp, G.; Schueler, C.F.; Fafaul, B.A.; Hansen, J.E.; Hooker, R.J.; Itchkawich, T.; Maring, H.B.; Travis, L.D. Accurate Monitoring of Terrestrial Aerosols and Total Solar Irradiance: Introducing the Glory Mission. *Am. Meteorol. Soc.* **2007**, *88*, 677–692. [CrossRef]
50. Ding, S.; Wang, J.; Xu, X. Polarimetric remote sensing in oxygen A and B bands: sensitivity study and information content analysis for vertical profile of aerosols. *Atmos. Meas. Tech.* **2016**, *9*, 2077–2092. [CrossRef]
51. Dubovik, O.; Holben, B.; Eck, T.F.; Smirnov, A.; Kaufman, Y.J.; King, M.D.; Tanré, D.; Slutsker, I. Variability of Absorption and Optical Properties of Key Aerosol Types Observed in Worldwide Locations. *J. Atmos. Sci.* **2002**, *59*, 590–608. [CrossRef]
52. Dubovik, O.; King, M.D. A flexible inversion algorithm for retrieval of aerosol optical properties from Sun and sky radiance measurements. *J. Geophys. Res. Biogeosci.* **2000**, *105*, 20673–20696. [CrossRef]
53. Hou, W.; Wang, J.; Xu, X.; Reid, J.S.; Han, D. An algorithm for hyperspectral remote sensing of aerosols: 1. Development of theoretical framework. *J. Quant. Spectrosc. Radiat. Transf.* **2016**, *178*, 400–415. [CrossRef]
54. Dubovik, O.; Smirnov, A.; Holben, B.N.; King, M.D.; Kaufman, Y.J.; Eck, T.F.; Slutsker, I. Accuracy assessments of aerosol optical properties retrieved from Aerosol Robotic Network (AERONET) Sun and sky radiance measurements. *J. Geophys. Res. Biogeosci.* **2000**, *105*, 9791–9806. [CrossRef]
55. Guerlet, S.; Butz, A.; Schepers, D.; Basu, S.; Hasekamp, O.P.; Kuze, A.; Yokota, T.; Blavier, J.-F.; Deutscher, N.M.; Griffith, D.W.T.; et al. Impact of aerosol and thin cirrus on retrieving and validating XCO_2 from GOSAT shortwave infrared measurements. *J. Geophys. Res. Atmos.* **2013**, *118*, 4887–4905. [CrossRef]